

Two Peculiar Fast Transients in a Strongly Lensed Host Galaxy

S. A. Rodney¹, I. Balestra², M. Bradač³, G. Brammer⁴, T. Broadhurst^{5,6}, G. B. Caminha⁷, G. Chirivì⁸, J. M. Diego⁹, A. V. Filippenko¹⁰, R. J. Foley¹¹, O. Graur^{12,13,14}, C. Grillo^{15,16}, S. Hemmati¹⁷, J. Hjorth¹⁶, A. Hoag³, M. Jauzac^{18,19,20}, S. W. Jha²¹, R. Kawamata²², P. L. Kelly¹⁰, C. McCully^{23,24}, B. Mobasher²⁵, A. Molino^{26,27}, M. Oguri^{28,29,30}, J. Richard³¹, A. G. Riess^{32,4}, P. Rosati⁷, K. B. Schmidt^{24,33}, J. Selsing¹⁶, K. Sharon³⁴, L.-G. Strolger⁴, S. H. Suyu^{8,35,36}, T. Treu^{37,38}, B. J. Weiner³⁹, L. L. R. Williams⁴⁰ & A. Zitrin⁴¹

A massive galaxy cluster can serve as a magnifying glass for distant stellar populations, with strong gravitational lensing exposing details in the lensed background galaxies that would otherwise be undetectable. The MACS J0416.1-2403 cluster (hereafter MACS0416) is one of the most efficient lenses in the sky, and in 2014 it was observed with high-cadence imaging from the Hubble Space Telescope (*HST*). Here we describe two unusual transient events that appeared behind MACS0416 in a strongly lensed galaxy at redshift $z = 1.0054 \pm 0.0002$. These transients—designated HFF14Spo-NW and HFF14Spo-SE and collectively nicknamed “Spock”—were faster and fainter than any supernova (SN), but significantly more luminous than a classical nova. They reached peak luminosities of $\sim 10^{41}$ erg s⁻¹ ($M_{AB} < -14$ mag) in $\lesssim 5$ rest-frame days, then faded below detectability in roughly the same time span. Models of the cluster lens suggest that these events may be *spatially* coincident at the source plane, but are most likely not *temporally* coincident. We find that HFF14Spo can be explained as a luminous blue variable (LBV), a recurrent nova (RN), or a pair of stellar microlensing events. To distinguish between these hypotheses will require a clarification of the positions of nearby critical curves, along with high-cadence monitoring of the field that could detect new transient episodes in the host galaxy.

¹Department of Physics and Astronomy, University of South Carolina, 712 Main St., Columbia, SC 29208, USA

²University Observatory Munich, Scheinerstrasse 1, D-81679 Munich, Germany

³University of California Davis, 1 Shields Avenue, Davis, CA 95616

⁴Space Telescope Science Institute, 3700 San Martin Dr., Baltimore, MD 21218, USA

⁵Fisika Teorikoa, Zientzia eta Teknologia Fakultatea, Euskal Herriko Unibertsitatea UPV/EHU

⁶IKERBASQUE, Basque Foundation for Science, Alameda Urquijo, 36-5 48008 Bilbao, Spain

⁷Dipartimento di Fisica e Scienze della Terra, Università degli Studi di Ferrara, via Saragat 1, I-44122, Ferrara, Italy

⁸Max-Planck-Institut für Astrophysik, Karl-Schwarzschild-Str. 1, 85748 Garching, Germany

⁹IFCA, Instituto de Física de Cantabria (UC-CSIC), Av. de Los Castros s/n, 39005 Santander, Spain

¹⁰Department of Astronomy, University of California, Berkeley, CA 94720-3411, USA

¹¹Department of Astronomy and Astrophysics, University of California, Santa Cruz, CA 95064, USA

¹²Center for Cosmology and Particle Physics, New York University, New York, NY 10003, USA

- ¹³*Department of Astrophysics, American Museum of Natural History, Central Park West and 79th Street, New York, NY 10024, USA*
- ¹⁴*Harvard/Smithsonian Center for Astrophysics, Cambridge, MA 02138, USA*
- ¹⁵*Dipartimento di Fisica, Università degli Studi di Milano, via Celoria 16, I-20133 Milano, Italy*
- ¹⁶*Dark Cosmology Centre, Niels Bohr Institute, University of Copenhagen, Juliane Maries Vej 30, DK-2100 Copenhagen, Denmark*
- ¹⁷*Cahill Center for Astronomy and Astrophysics, California Institute of Technology, MC 249-17, Pasadena, CA 91125, USA*
- ¹⁸*Centre for Extragalactic Astronomy, Department of Physics, Durham University, Durham DH1 3LE, U.K.*
- ¹⁹*Institute for Computational Cosmology, Durham University, South Road, Durham DH1 3LE, U.K.*
- ²⁰*Astrophysics and Cosmology Research Unit, School of Mathematical Sciences, University of KwaZulu-Natal, Durban 4041, South Africa*
- ²¹*Department of Physics and Astronomy, Rutgers, The State University of New Jersey, Piscataway, NJ 08854, USA*
- ²²*Department of Astronomy, Graduate School of Science, The University of Tokyo, 7-3-1 Hongo, Bunkyo-ku, Tokyo 113-0033, Japan*
- ²³*Las Cumbres Observatory Global Telescope Network, 6740 Cortona Dr., Suite 102, Goleta, California 93117, USA*
- ²⁴*Department of Physics, University of California, Santa Barbara, CA 93106-9530, USA*
- ²⁵*Department of Physics and Astronomy, University of California, Riverside, CA 92521, USA*
- ²⁶*Instituto de Astronomia, Geofísica e Ciências Atmosféricas, Universidade de São Paulo, Cidade Universitária, 05508-090, São Paulo, Brazil*
- ²⁷*Instituto de Astrofísica de Andalucía (CSIC), E-18080 Granada, Spain*
- ²⁸*Research Center for the Early Universe, University of Tokyo, 7-3-1 Hongo, Bunkyo-ku, Tokyo 113-0033, Japan*
- ²⁹*Department of Physics, University of Tokyo, 7-3-1 Hongo, Bunkyo-ku, Tokyo 113-0033, Japan*
- ³⁰*Kavli Institute for the Physics and Mathematics of the Universe (Kavli IPMU, WPI), University of Tokyo, 5-1-5 Kashiwanoha, Kashiwa, Chiba 277-8583, Japan*
- ³¹*Université Lyon, Univ Lyon1, Ens de Lyon, CNRS, Centre de Recherche Astrophysique de Lyon UMR5574, F-69230, Saint-Genis-Laval, France*
- ³²*Department of Physics and Astronomy, The Johns Hopkins University, 3400 N. Charles St., Baltimore, MD 21218, USA*
- ³³*Leibniz-Institut für Astrophysik Potsdam (AIP), An der Sternwarte 16, 14482 Potsdam, Germany*
- ³⁴*Department of Astronomy, University of Michigan, 1085 S. University Avenue, Ann Arbor, MI 48109, USA*
- ³⁵*Institute of Astronomy and Astrophysics, Academia Sinica, P.O. Box 23-141, Taipei 10617, Taiwan*
- ³⁶*Physik-Department, Technische Universität München, James-Franck-Straße 1, 85748 Garching, Germany*
- ³⁷*Department of Physics and Astronomy, University of California, Los Angeles, CA 90095*

³⁸Packard Fellow

³⁹Department of Astronomy, University of Arizona, Tucson, AZ 85721, USA

⁴⁰School of Physics and Astronomy, University of Minnesota, 116 Church Street SE, Minneapolis, MN 55455, USA

⁴¹Ben-Gurion University of the Negev P.O.B. 653 Beer-Sheva 8410501, Israel

When a star explodes or a relativistic jet erupts from near the edge of a black hole, the event can be visible across many billions of light-years. Such extremely luminous astrophysical transients as supernovae (SNe), gamma-ray bursts, and quasars are powerful tools for probing cosmic history and sampling the matter and energy content of the universe. Less energetic transients generated by the tumultuous atmospheres of massive stars or the interactions of close stellar binaries are also very valuable for understanding stellar evolution and the physical processes that lead to stellar explosions. However, the lower luminosity of such events makes them accessible only in the local universe, and consequently our census of peculiar transients at the stellar scale is still highly incomplete.

Although recent surveys are beginning to discover progressively more categories of rapidly changing optical transients^{1,2}, most programs remain largely insensitive to transients with peak brightness and timescales comparable to the HFF14Spo events³. Future wide-field observatories such as the Large Synoptic Survey Telescope⁴ will be much more efficient at discovering such transients, and can be expected to reveal many new categories of astrophysical transients.

As shown in Figure 1, the HFF14Spo events appeared in *HST* imaging collected as part of the Hubble Frontier Fields (HFF) survey⁵, a multi-cycle program for deep imaging of 6 massive galaxy clusters and associated “blank sky” fields observed in parallel. *HST* is not an efficient wide-field survey telescope, and the HFF survey was not designed with the discovery of peculiar extragalactic transients as a core objective. However, the HFF program has unintentionally opened an effective window of discovery for such events. Very faint sources at relatively high redshift ($z \gtrsim 1$) in these fields are made detectable by the substantial gravitational lensing magnification from the foreground galaxy clusters. Very rapidly evolving sources are also more likely to be found, owing to the necessity of a rapid cadence for repeat imaging in the HFF program.

1 Results

To evaluate the impact of gravitational lensing from the MACS0416 cluster on the observed light curves and the timing of these two events, we use seven independently constructed cluster mass models. These models indicate that the gravitational time delay between the HFF14Spo-NW location and the HFF14Spo-SE location is <60 days (Table 1). This falls far short of the observed 223 day span between the two events, suggesting that HFF14Spo-SE is not a time-delayed image of the HFF14Spo-NW event. As shown in Figure 2, HFF14Spo-NW and HFF14Spo-SE are inconsistent with these predicted time delays if one assumes that they are delayed images of a single event. However, if these were independent events, then a time delay on the order of tens of days between image 11.1 and 11.2 could have resulted in time-delayed events that were missed by the *HST* imaging of this field.

The models also predict absolute magnification values between about $\mu = 10$ and $\mu = 200$ for both events. This wide range is due primarily to the close proximity of the lensing critical curve

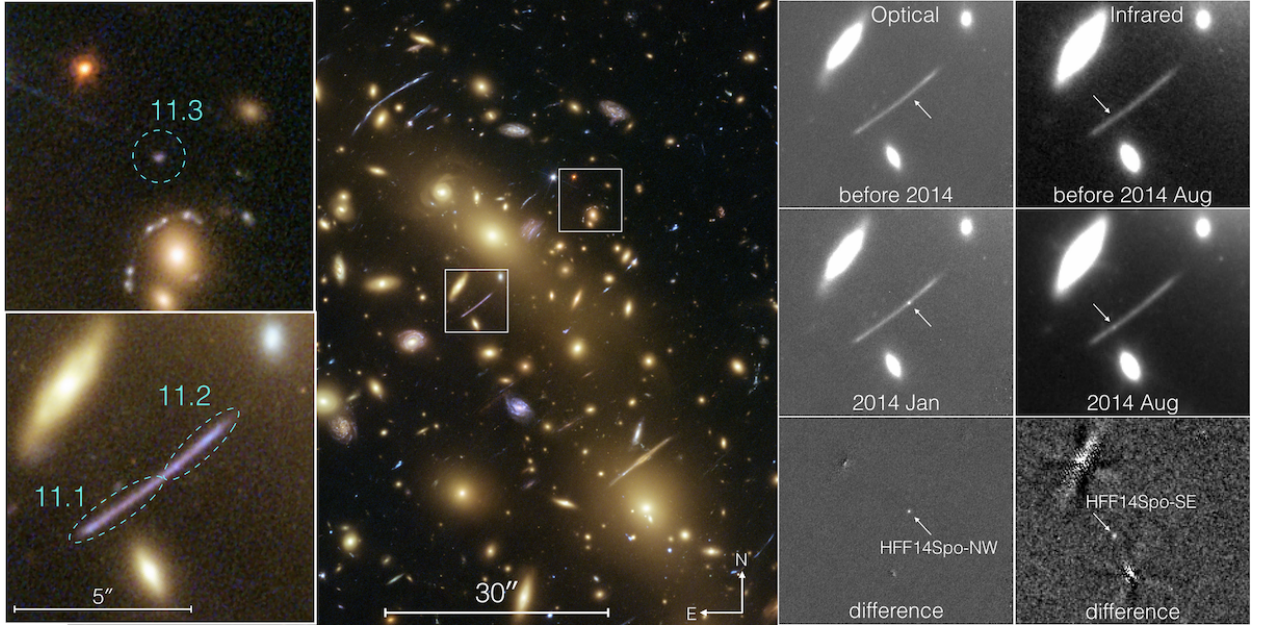


Figure 1: The detection of HFF14Spo-NW and HFF14Spo-SE in *HST* imaging from the Hubble Frontier Fields. The central panel shows the full field of the MACSJ0416 cluster, in a combined image using optical and infrared bands from *HST*. Two boxes within the main panel demarcate the regions where the HFF14Spo host-galaxy images appear. These regions are shown as two inset panels on the left, highlighting the three images of the host galaxy (labeled 11.1, 11.2, and 11.3), which are caused by the gravitational lensing of the cluster. Two columns on the right side show the discovery of the two transient events in optical and infrared light, respectively. In these final two columns the top row is a template image, the center row shows the epoch when each transient appeared, and the bottom row is the difference image.

Table 1. Lens model predictions for time delays and magnifications at the observed locations of the HFF14Spo transients.

Model	$ \mu_{\text{NW}} $	$ \mu_{\text{SE}} $	$ \mu_{11.3} $	$\Delta t_{\text{NW:SE}}$ (days)	$\Delta t_{\text{NW:11.3}}$ (years)
CATS	196^{+140}_{-53}	46^{+2}_{-1}	$3.3^{+0.0}_{-0.0}$	$-1.7^{+2.0}_{-1.9}$	$-3.7^{+0.1}_{-0.2}$
GLAFIC	29^{+43}_{-10}	84^{+103}_{-38}	$3.0^{+0.2}_{-0.2}$	$4.1^{+5.5}_{-3.4}$	$-5.0^{+0.5}_{-0.6}$
GLEE	182^{+203}_{-83}	67^{+31}_{-16}	$2.9^{+0.1}_{-0.1}$	36^{+6}_{-7}	$-6.1^{+0.3}_{-0.2}$
GRALE	13^{+11}_{-6}	12^{+9}_{-5}	$3.1^{+2.2}_{-0.9}$	-10^{+1}_{-7}	$-2.5^{+1.0}_{-3.1}$
SWunited	38 ± 8	13 ± 1	2.9 ± 0.1
WSLAP ⁺	35 ± 20	30 ± 20	...	-48 ± 10	0.8
ZLTM	103^{+48}_{-40}	32^{+8}_{-10}	3.5 ± 0.3	43^{+12}_{-10}	-3.7 ± 0.3

Note. — Each lens model is identified by the name of the modeling team or tool. Time delays give the predicted delay relative to an appearance in the NW host image, 11.2. Positive (negative) values indicate the NW image is the leading (trailing) image of the pair. The observed time lag between the NW and SE events was $\Delta t_{\text{NW:SE}} = 234 \pm 6$ days.

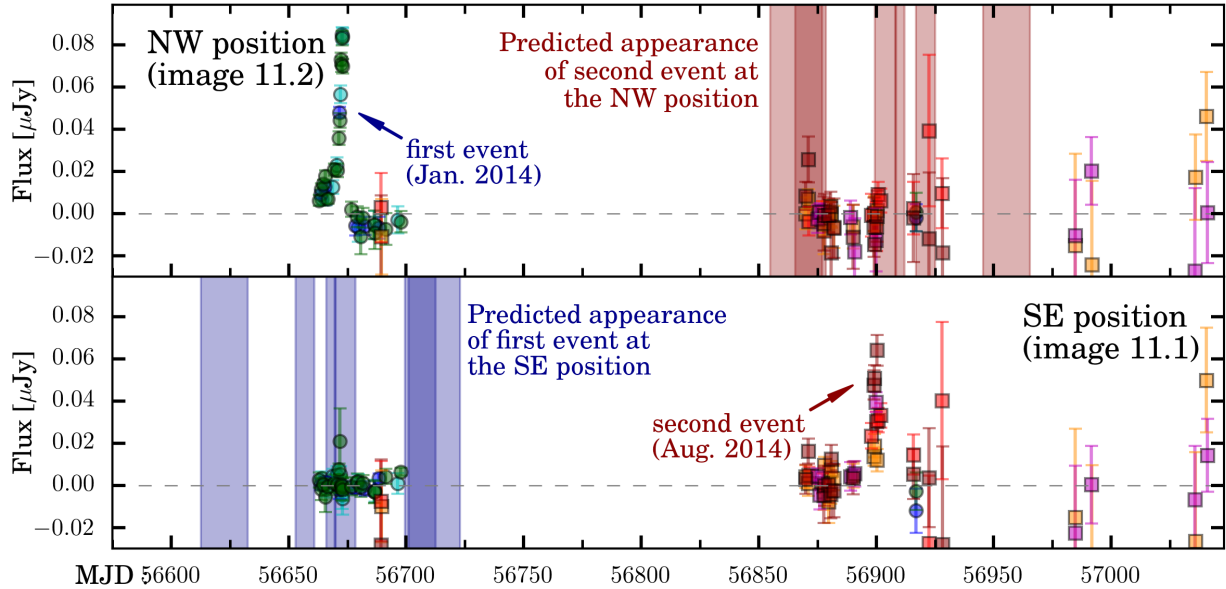


Figure 2: Predictions for the reappearance episodes of both HFF14Spo-NW and HFF14Spo-SE due to gravitational lensing time delays, as listed in Table 1. The top panel shows photometry collected at the NW position (host-galaxy image 11.2) where the first event (HFF14Spo-NW) appeared in January, 2014. Optical measurements from ACS are in blue and green, and infrared observations from WFC3-IR are in red and orange. Each blue bar in the lower panel shows one lens model prediction for the dates when that same physical event (HFF14Spo-NW) would have also appeared in the SE location (galaxy image 11.1), due to gravitational lensing time delay. The lower panel plots photometry from the SE position (11.1). On the right side we see the second observed event (HFF14Spo-SE). The red bars above show model predictions for when the NW host image 11.2 would have exhibited the gravitationally delayed image of the HFF14Spo-SE event. The width of each bar encompasses the 68% confidence region for a single model, and darker regions indicate an overlap from multiple models.

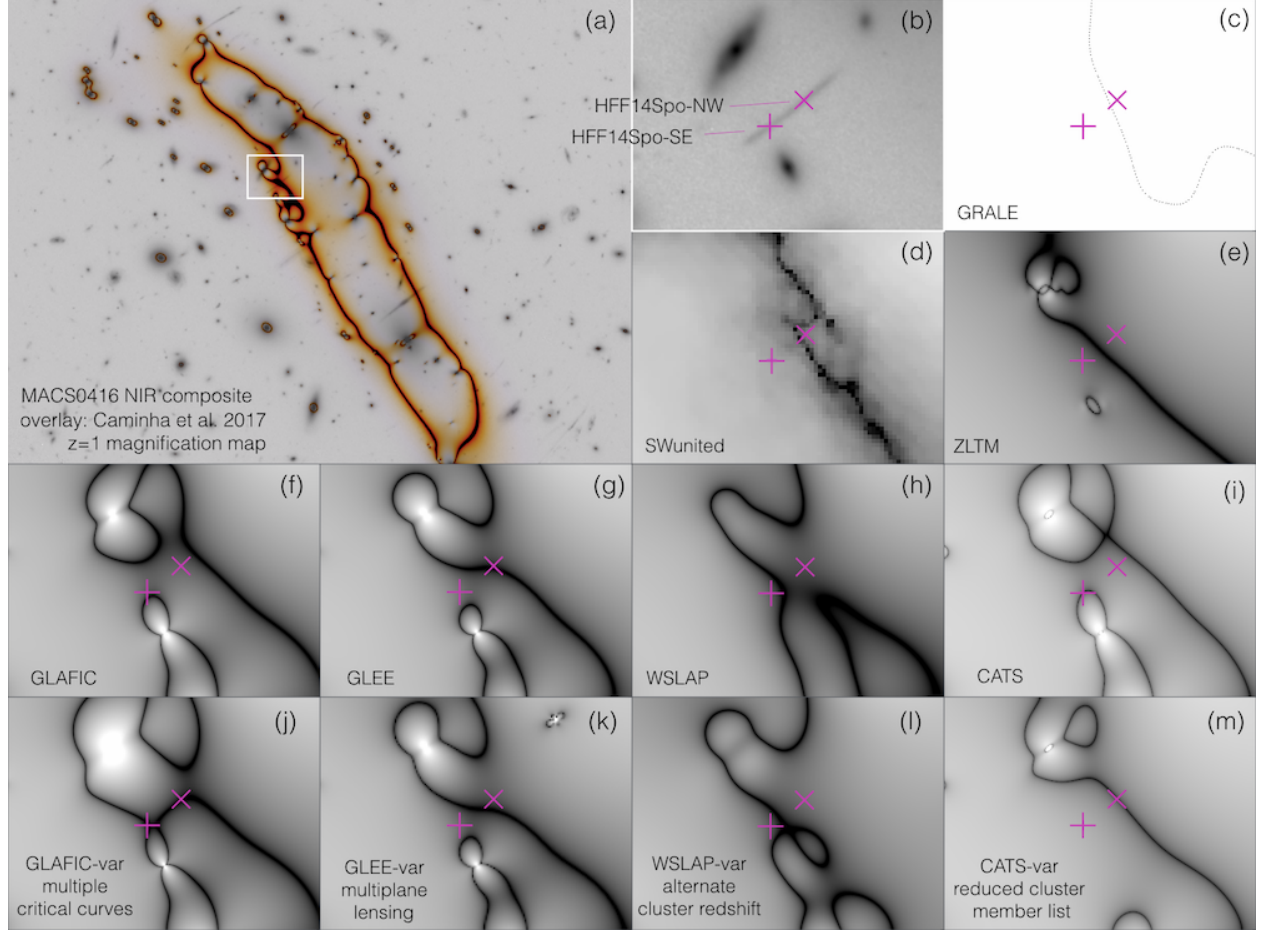


Figure 3: Locations of the lensing critical curves relative to the positions of the two HFF14Spo sources. Panel (a) shows the *HST* Frontier Fields composite near-infrared image of the full MACS0416 field. The magnification map for a source at $z = 1$ is overlaid with orange and black contours⁶. The white box marks the region that is shown in panel (b) with a closer view of the HFF14Spo host galaxy. Panel (c) shows a trace of the lensing critical curve from the GRALE model, and panels (d)-(i) show magnification maps for the six other primary models, all for a source at the HFF14Spo redshift. The magnification maps are plotted with log scaling, such that white is $\mu = 1$ and black is $\mu = 10^3$. Panels j-m show the same magnification maps, extracted from the lens model variations (see Methods).

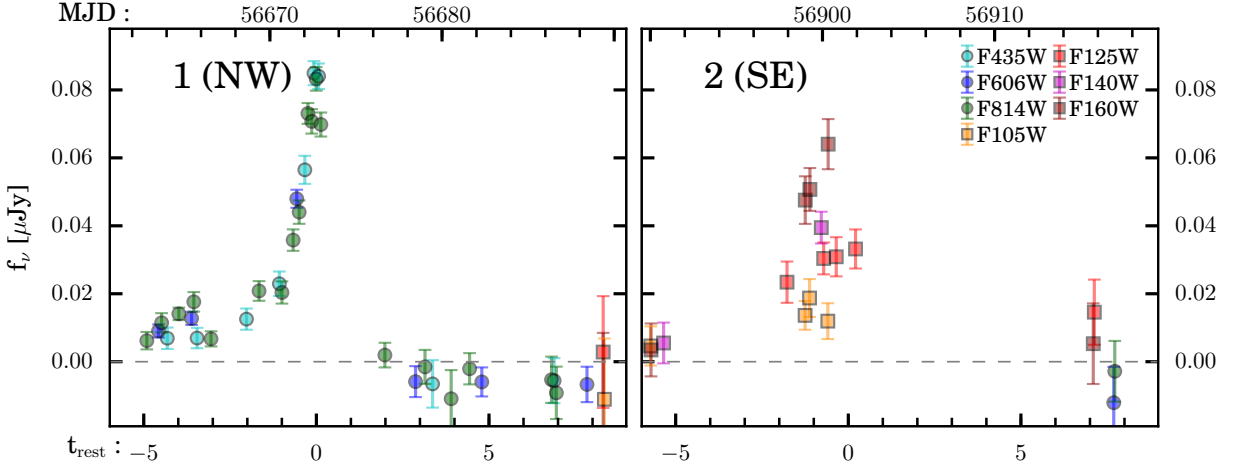


Figure 4: Light curves for the two transient events, HFF14Spo-NW on the left and HFF14Spo-SE on the right. Measured fluxes in micro-Janskys are plotted against rest-frame time at $z = 1.0054$, relative to the time of the peak observed flux for each event. The corresponding Modified Julian Date (MJD) in the observer frame is marked on the top axis for each panel. As indicated in the legend, optical observations using the *HST* ACS-WFC detector are plotted as circles, while infrared measurements from the WFC3-IR detector are plotted as squares.

(the region of theoretically infinite magnification) for sources at $z = 1$. The lensing configuration consistently adopted for this cluster assumes that the arc comprises two mirror images of the host galaxy (labeled 11.1 and 11.2 in Figure 1)^{6,9–16}. This implies that a single critical curve passes roughly midway between the two HFF14Spo locations. The location of the critical curve varies significantly among the models (Figure 3), and is sensitive to many parameters that are poorly constrained. We find that it is possible to make reasonable adjustments to the lens model parameters so that the critical curve does not bisect the HFF14Spo host arc, but instead intersects both of the HFF14Spo locations (see Supplementary Note 2). Such lensing configurations can qualitatively reproduce the observed morphology of the HFF14Spo host galaxy, but they are disfavored by a purely quantitative assessment of the positional strong-lensing constraints.

Ruling Out Common Astrophysical Transients. There are several categories of astrophysical transients that can be rejected based solely on characteristics of the HFF14Spo-NW and HFF14Spo-SE light curves, shown in Figure 4. Neither of the HFF14Spo events is *periodic*, as expected for stellar pulsations such as Cepheids, RR Lyrae, or Mira variables. Stellar flares can produce rapid optical transient phenomena, but the total energy released by even the most extreme stellar flare¹⁷ falls far short of the observed energy release from the HFF14Spo transients. We can also rule out active galactic nuclei (AGN), which are disfavored by the quiescence of the HFF14Spo sources between the two observed episodes and the absence of any of the broad emission lines that are often observed in AGN. Additionally, no x-ray emitting point source was detected in 7 epochs from 2009 to 2014, including *Chandra* X-ray Space Telescope imaging that was coeval with the peak of infrared emission from HFF14Spo-SE.

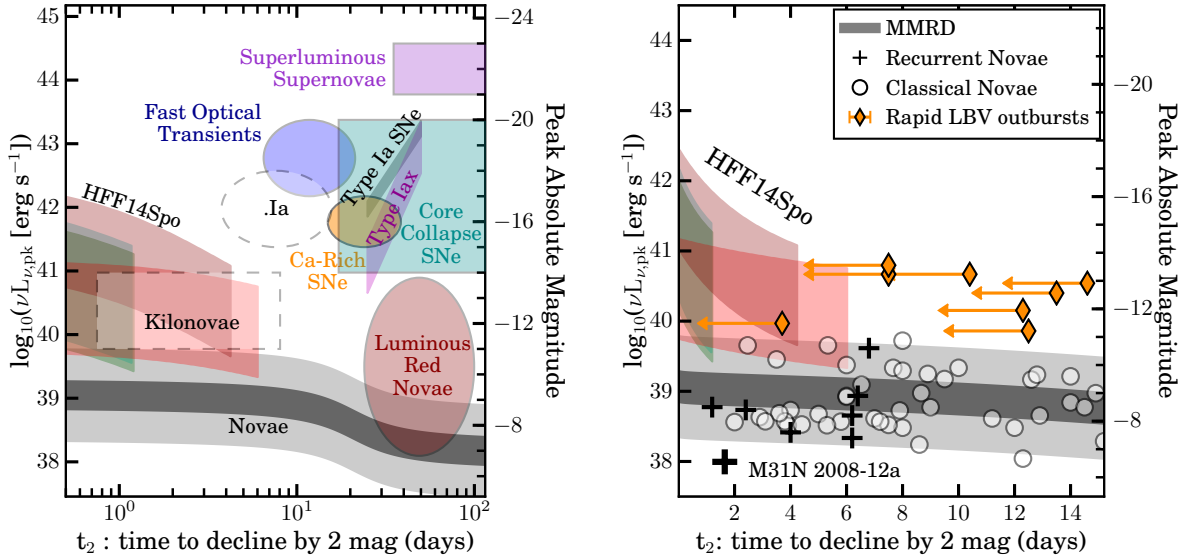


Figure 5: Peak luminosity vs. decline time for HFF14Spo and assorted categories of explosive transients. Observed constraints of the HFF14Spo events are plotted as overlapping colored bands, along the left side of the figure. HFF14Spo-NW is shown as cyan and blue bands, corresponding to independent constraints drawn from the F435W and F814W light curves, respectively. For HFF14Spo-SE the scarlet and maroon bands show constraints from the F125W and F160W light curves, respectively. The width and height of these bands incorporates the uncertainty due to magnification (we adopt $7 < \mu_{\text{NW}} < 485$ and $7 < \mu_{\text{SE}} < 185$; see Table 1) and the time of peak. In the left panel, ellipses and rectangles mark the luminosity and decline-time regions occupied by various explosive transient classes. Filled shapes show the empirical bounds for transients with a substantial sample of known events. Dashed regions mark theoretical expectations for rare transients that lack a significant sample size: the ‘‘Ia’’ class of white dwarf He shell detonations and the kilonova class from neutron star mergers. Grey bands in both panels show the MMRD relation for classical novae. In the right panel, circles mark the observed peak luminosities and decline times for classical novae, while black ‘+’ symbols mark recurrent novae from our own Galaxy. The large cross labeled at the bottom shows the rapid recurrence nova M31N 2008-12a. Each orange diamond marks a separate short transient event from the two rapid LBV outburst systems, SN 2009ip⁷ and NGC3432-LBV1 (also known as SN 2000ch)⁸. These LBV events provide only upper limits on the decline time owing to limited photometric sampling.

Many types of stellar explosions can generate isolated transient events, and a useful starting point for classification of such objects is to examine their position in the phase space of peak luminosity (L_{pk}) versus decline time¹⁸. Figure 5 shows our two-dimensional constraints on L_{pk} and the decline timescale t_2 (the time over which the transient declines by 2 mag) for the HFF14Spo events, accounting for the range of lensing magnifications ($10 < \mu < 200$) derived from the cluster lens models. The HFF14Spo-NW and HFF14Spo-SE events are largely consistent with each other, and if both events are representative of a single system (or a homogeneous class) then the most likely peak luminosity and decline time (the region with the most overlap) would be $L_{\text{pk}} \approx 10^{41}$ erg s⁻¹ and $t_2 \approx 1$ day.

The relatively low peak luminosities and the very rapid rise and fall of both HFF14Spo light curves are incompatible with all categories of stellar explosions for which a significant sample of observed events exists. This includes the common Type Ia SNe and core-collapse SNe, as well as the less well-understood classes of superluminous SNe¹⁹, Type Iax SNe²⁰, fast optical transients², Ca-rich SNe²¹, and luminous red novae¹⁸.

The SN-like transients that come closest to matching the observed light curves of the two HFF14Spo events are the “kilonova” class and the “.Ia” class. Kilonovae are a theorized category of optical/near-infrared transients that may be generated by the merger of a neutron star (NS) binary²². The .Ia class is produced by He shell explosions that are expected to arise from AM Canum Venaticorum (AM CVn) binary star systems undergoing He mass transfer onto a white dwarf primary star^{23,24}. The HFF14Spo light curves exhibited a slower rise time than is expected for a kilonova event^{25–27}, and a faster decline time than is anticipated for a .Ia event²⁸.

Another problem for all of these catastrophic stellar explosion models is that they cannot explain the appearance of *repeated* transient events. The kilonova progenitor systems are completely disrupted at explosion, as is the case for all normal SN explosions. For .Ia events, even if an AM CVn system could produce repeated He shell flashes of similar luminosity, the period of recurrence would be $\sim 10^5$ yr, making these effectively non-recurrent sources.

Although the two events were most likely not *temporally* coincident, all of our lens models indicate that it is entirely plausible for the two HFF14Spo events to be *spatially* coincident: a single location at the source plane can be mapped to both HFF14Spo locations to within the positional accuracy of the model reconstructions ($\sim 0.6''$ in the lens plane). This is supported by the fact that the host-galaxy colors and spectral indices at each HFF14Spo location are indistinguishable within the uncertainties (see Supplementary Figure 4 and Supplementary Table 2). Thus, to accommodate all of the observations of the HFF14Spo events with a single astrophysical source, we turn to two categories of stellar explosion that are sporadically recurrent: luminous blue variables (LBVs) and recurrent novae (RNe).

Luminous Blue Variable. The transient sources categorized as LBVs are the result of eruptions or explosive episodes from massive stars ($> 10 M_\odot$). The class is exemplified by examples such as P Cygni, η Carinae (η Car), and S Doradus^{29,30}. Although most giant LBV eruptions have been observed to last much longer than the HFF14Spo events²⁹, some LBVs have exhibited repeated rapid outbursts that are broadly consistent with the very fast HFF14Spo light curves (see Supplementary Figure 6). Because of this common stochastic variability, the LBV hypothesis does not have any trouble accounting for the HFF14Spo events as two separate episodes.

Two well-studied LBVs that provide a plausible match to the observed HFF14Spo events are “SN 2009ip”³¹ and NGC3432-LBV1⁸. Both exhibited multiple brief transient episodes over a span of months to years^{8,32–34}. Unfortunately, for these outbursts we have only upper limits on the decline timescale, t_2 , owing to the relatively sparse photometric sampling. Recent studies have shown that SN 2009ip-like LBV transients have remarkably similar light curves, leading up to a final terminal SN explosion^{35,36}. Figure 5b shows that both HFF14Spo events are consistent with the observed luminosities and decline times of these fast and bright LBV outbursts – though the HFF14Spo events would be among the most rapid and most luminous LBV eruptions ever seen.

In addition to those relatively short and very bright giant eruptions, most LBVs also commonly exhibit a slower underlying variability. P Cygni and η Car, for example, slowly rose and fell in brightness by ~ 1 to 2 mag over a timespan of several years before and after their historic giant eruptions. Such variation has not been detected at the HFF14Spo locations. Nevertheless, given the broad range of light-curve behaviors seen in LBV events, we cannot reject this class as a possible explanation for the HFF14Spo system.

The total radiated energy of the HFF14Spo events is in the range $10^{44} < E_{\text{rad}} < 10^{47}$ erg (see Methods), which falls well within the range of plausible values for a major LBV outburst. From this measurement we can derive constraints on the luminosity of the progenitor star, by assuming that the energy released is generated slowly in the stellar interior and is in some way “bottled up” by the stellar envelope, before being released in a rapid mass ejection (see Methods). With this approach we find a quiescent luminosity of $L_{\text{qui}} \approx 10^{39.5}$ erg s⁻¹ ($M_V \approx -10$ mag). This value is fully consistent with the expected range for LBV progenitor stars (e.g., η Car has $M_V \approx -12$ mag and the faintest known LBV progenitors such as SN 2010dn have $M_V \approx -6$ mag).

Recurrent Nova. Novae occur in binary systems in which a white dwarf star accretes matter from a less massive companion, leading to a burst of nuclear fusion in the accreted surface layer that causes the white dwarf to brighten by several orders of magnitude, but does not completely disrupt the star. The mass transfer from the companion to the white dwarf may restart after the explosion, so the cycle may begin again and repeat after a period of months or years. When this recurrence cycle is directly observed, the object is classified as a recurrent nova (RN).

The light curves of many RN systems in the Milky Way are similar in shape to the HFF14Spo episodes, exhibiting a sharp rise (< 10 days in the rest-frame) and a similarly rapid decline (see Supplementary Information and Supplementary Figure 7). This is reflected in Figure 5, where novae are represented by a grey band that traces the empirical constraints on the maximum magnitude vs. rate of decline (MMRD) relation for classical novae^{1,37–39}.

The RN model can provide a natural explanation for having two separate explosions that are coincident in space but not in time. However, the recurrence timescale for HFF14Spo in the rest frame is 120 ± 30 days, which would be a singularly rapid recurrence period for a RN system. The RNe in our own Galaxy have recurrence timescales of 10–98 years⁴⁰. The fastest measured recurrence timescale belongs to M31N 2008-12a, which has exhibited a new outburst every year from 2008 through 2016^{41–45}. Although this M31 record-holder demonstrates that very rapid recurrence is possible, classifying HFF14Spo as a RN would still require a very extreme mass-transfer rate to accommodate the < 1 year recurrence.

Another major concern with the RN hypothesis is that the two HFF14Spo events are sub-

stantially brighter than all known novae—perhaps by as much as 2 orders of magnitude. This is exacerbated by the observational and theoretical evidence indicating that rapid-recurrence novae have less energetic eruptions⁴⁶ (see Supplementary Information and Supplementary Figure 8). Although the RN model is not strictly ruled out, we can deduce that if the HFF14Spo transients are caused by a single RN system, then that progenitor system would be among the most extreme white dwarf binary systems yet known.

Microlensing. In the presence of strong gravitational lensing it is possible to generate a transient event from lensing effects alone. In this case the background source has a steady luminosity but the relative motion of the source, lens, and observer causes the magnification of that source (and therefore the apparent brightness) to change rapidly with time. An isolated strong lensing event with a rapid timescale can be generated when a background star crosses over a lensing caustic (the mapping of the critical curve back on to the source plane). In the case of a star crossing the caustic of a smooth lensing potential, the amplification of the source flux would increase (decrease) with a characteristic $t^{-1/2}$ profile as it moves toward (away from) the caustic. This slowly evolving light curve then transitions to a very sharp decline (rise) when the star has moved to the other side of the caustic^{47,48}. With a more complex lens comprising many compact objects, the light curve would exhibit a superposition of many such sharp peaks^{49,50}.

The peculiar transient MACS J1149 LS1, observed behind the Hubble Frontier Fields cluster MACS J1149.6+2223, has been proposed as the first observed example of such a stellar caustic crossing event⁵¹. Such events may be expected to appear more frequently in strongly lensed galaxies that have small angular separation from the center of a massive cluster. In such a situation, our line of sight to the lensed background galaxy passes through a dense web of overlapping microlenses caused by the intracluster stars distributed around the center of the cluster. This has the effect of “blurring” the magnification profile across the cluster critical curve, making it more likely that a single (and rare) massive star in the background galaxy gets magnified by the required factor of $\sim 10^5$ to become visible as a transient caustic-crossing event. On this basis the HFF14Spo host-galaxy images are suitably positioned for caustic-crossing transients, as they are seen through a relatively high density of intracluster stars (see Methods)—comparable to that observed for the MACS J1149 LS1 transient.

The characteristic timescale of a canonical caustic-crossing event would be on the order of hours or days (see Supplementary Information), which is comparable to the timescales observed for the HFF14Spo events. Gravitational lensing is achromatic as long as the size of the source is consistent across the spectral energy distribution (SED). This means that the color of a caustic-crossing transient will be roughly constant. Using simplistic linear interpolations of the observed light curves (see Methods), we find that the inferred color curves for both HFF14Spo events are marginally consistent with this expectation of an unchanging color (Supplementary Figure 9).

In the baseline lensing configuration adopted above—where a single critical curve subtends the HFF14Spo host galaxy arc—these events cannot plausibly be explained as stellar caustic crossings, because neither transient is close enough to the single critical curve to reach the required magnifications of $\mu \approx 10^6$. Some of our lens models can, however, be modified so that instead of just two host images, the lensed galaxy arc is made up of many more images of the host, with multiple critical curves subtending the arc where the HFF14Spo events appeared (Figure 3). If this

alternative lensing situation is correct, then similar microlensing transients would be expected to appear at different locations along the host-galaxy arc, instigated by new caustic-crossing episodes from different stars in the host galaxy.

The Rate of Similar Transients. Although we lack a definitive classification for these events, we can derive a simplistic estimate of the rate of HFF14Spo-like transients by counting the number of strongly lensed galaxies in the HFF clusters that have sufficiently high magnification that a source with $M_V = -14$ mag would be detected in *HST* imaging. There are only six galaxies that satisfy that criteria, all with $0.5 < z < 1.5$ (Methods). Each galaxy was observed by the high-cadence HFF program for an average of 80 days. Treating HFF14Spo-NW and HFF14Spo-SE as separate events leads to a very rough rate estimate of 1.5 HFF14Spo-like events per galaxy per year.

Derivation of a volumetric rate for such events would require a detailed analysis of the lensed volume as a function of redshift, and is beyond the scope of this work. Nevertheless, a comparison to rates of similar transients in the local universe can inform our assessment of the likelihood that the HFF14Spo events are unrelated. A study of very fast optical transients with the Pan-STARRS1 survey derived a rate limit of $\lesssim 0.05 \text{ Mpc}^{-3} \text{ yr}^{-1}$ for transients reaching $M \approx -14$ mag on a timescale of ~ 1 day³. This limit, though several orders of magnitude higher than the constraints on novae or SNe, is sufficient to make it exceedingly unlikely that two unrelated fast optical transients would appear in the same galaxy in a single year. Furthermore, we have observed no other transient events with similar luminosities and light curve shapes in high-cadence surveys of five other Frontier Fields clusters. Indeed, all other transients detected in the primary HFF survey have been fully consistent with normal SNe. Thus, we have no evidence to suggest that transients of this kind are common enough to be observed twice in a single galaxy in a single year.

2 Discussion

We have examined three plausible explanations for the HFF14Spo events: (1) they were separate rapid outbursts of an LBV star, (2) they were surface explosions from a single RN, or (3) they were each caused by the rapidly changing magnification as two unrelated massive stars crossed over lensing caustics. We cannot make a definitive choice between these hypotheses, principally due to the scarcity of observational data and the uncertainty in the location of the lensing critical curves.

If there is just a single critical curve for a source at $z = 1$ passing between the two HFF14Spo locations, then our preferred explanation for the HFF14Spo events is that we have observed two distinct eruptive episodes from a massive LBV star. In this scenario, the HFF14Spo LBV system would most likely have exhibited multiple eruptions over the last few years, but most of them were missed, as they landed within the large gaps of the *HST* Frontier Fields imaging program. The HFF14Spo events would be extreme LBV outbursts in several dimensions, and should add a useful benchmark for the outstanding theoretical challenge of developing a comprehensive physical model that accommodates both the η Car-like great eruptions and the S Dor-type variation of LBVs.

If instead the MACS0416 lens has multiple critical curves that intersect both HFF14Spo locations, then the third proposal of a microlensing-generated transient would be preferred. Stellar caustic crossings have not been observed before, but the analysis of a likely candidate behind the MACSJ1149 cluster suggests that massive cluster lenses may generate such events more frequently than previously expected^{50,51}. To resolve the uncertainty of the HFF14Spo classification will require refinement of the lens models to more fully address systematic biases and more tightly

constrain the path of the critical curve. High-cadence monitoring of the MACS0416 field would also be valuable, as it could catch future LBV eruptions or microlensing transients at or near these locations.

Methods

Discovery. The transient HFF14Spo was discovered in *HST* imaging collected as part of the Hubble Frontier Fields (HFF) survey (HST-PID: 13496, PI: Lotz), a multi-cycle program observing 6 massive galaxy clusters and associated “blank sky” parallel fields⁵. Several *HST* observing programs have provided additional observations supplementing the core HFF program. One of these is the FrontierSN program (HST-PID: 13386, PI: Rodney), which aims to identify and study explosive transients found in the HFF and related programs⁵². The FrontierSN team discovered HFF14Spo in two separate HFF observing campaigns on the galaxy cluster MACS0416. The first was an imaging campaign in January, 2014 during which the MACS0416 cluster field was observed in the F435W, F606W, and F814W optical bands using the Advanced Camera for Surveys Wide Field Camera (ACS-WFC). The second concluded in August, 2014, and imaged the cluster with the infrared detector of *HST*’s Wide Field Camera 3 (WFC3-IR) using the F105W, F125W, F140W, and F160W bands.

To discover transient sources, the FrontierSN team processes each new epoch of *HST* data through a difference-imaging pipeline (<https://github.com/srodney/sndrizpipe>), using archival *HST* images to provide reference images (templates) which are subtracted from the astrometrically registered HFF images. In the case of MACS0416, the templates were constructed from images collected as part of the Cluster Lensing And Supernova survey with Hubble (CLASH, HST-PID:12459, PI:Postman)⁵³. The resulting difference images are visually inspected for new point sources, and any new transients of interest (primarily SNe) are monitored with additional *HST* imaging or ground-based spectroscopic observations as needed.

Photometry. The follow-up observations for HFF14Spo included *HST* imaging observations in infrared and optical bands using the WFC3-IR and ACS-WFC detectors, respectively. Tables 3 and 4 present photometry of the HFF14Spo events from all available *HST* observations. The flux was measured on difference images, first using aperture photometry with a 0''.3 radius, and also by fitting with an empirical point spread function (PSF). The PSF model was defined using *HST* observations of the G2V standard star P330E, observed in a separate calibration program. A separate PSF model was defined for each filter, but owing to the long-term stability of the *HST* PSF we used the same model in all epochs. All of the aperture and PSF-fitting photometry was carried out using the PythonPhot software package (<https://github.com/djones1040/PythonPhot>)⁵⁴.

Host-Galaxy Spectroscopy. Spectroscopy of the HFF14Spo host galaxy was collected using three instruments on the Very Large Telescope (VLT). Observations with the VLT’s X-shooter cross-dispersed echelle spectrograph⁵⁵ were taken on October 19, 21 and 23, 2014 (Program 093.A-0667(A), PI: J. Hjorth) with the slit centered on the position of HFF14Spo-SE. The total integration time was 4.0 hours for the NIR arm of X-shooter, 3.6 hours for the VIS arm, and 3.9 hours for the UVB arm. The spectrum did not provide any detection of the transient source itself (as we will see below, it had already faded back to its quiescent state by that time). However, it did provide an unambiguous redshift for the host galaxy of $z = 1.0054 \pm 0.0002$ from H α and the [OII] doublet in data from the NIR and VIS arms, respectively. These line identifications are consistent with two

measures of the photometric redshift of the host: $z = 1.00 \pm 0.02$ from the BPZ algorithm⁵⁶, and $z = 0.92 \pm 0.05$ from the EAZY program⁵⁷. Both were derived from *HST* photometry of the host images 11.1 and 11.2, spanning 4350–16000 Å.

Additional VLT observations were collected using the Visible Multi-object Spectrograph (VIMOS)⁵⁸, as part of the CLASH-VLT large program (Program 186.A-0.798; P.I.: P. Rosati)⁵⁹, which collected \sim 4000 reliable redshifts over 600 arcmin² in the MACS0416 field^{14,60}. These massively multi-object observations could potentially have provided confirmation of the redshift of the HFF14Spo host galaxy with separate spectral line identifications in each of the three host-galaxy images. For the MACS0416 field the CLASH-VLT program collected 1 hour of useful exposure time in good seeing conditions with the Low Resolution Blue grism. Unfortunately, the wavelength range of this grism (3600–6700 Å) does not include any strong emission lines for a source at $z = 1.0054$, and the signal-to-noise ratio (S/N) was not sufficient to provide any clear line identifications for the three images of the HFF14Spo host galaxy.

The VLT Multi Unit Spectroscopic Explorer (MUSE)^{61,62} observed the NE portion of the MACS0416 field—where the HFF14Spo host images are located—in December, 2014 for 2 hours of integration time (ESO program 094.A-0115, PI: J. Richard). These observations also confirmed the redshift of the host galaxy with clear detection of the [OII] doublet. Importantly, since MUSE is an integral field spectrograph, these observations also provided a confirmation of the redshift of the third image of the host galaxy, 11.3, with a matching [OII] line at the same wavelength⁶.

A final source of spectroscopic information relevant to HFF14Spo is the Grism Lens Amplified Survey from Space (GLASS; PID: HST-GO-13459; PI:T. Treu)^{63,64}. The GLASS program collected slitless spectroscopy on the MACS0416 field using the WFC3-IR G102 and G141 grisms on *HST*, deriving redshifts for galaxies down to a magnitude limit $H < 23$. As with the VLT VIMOS data, the three sources identified as images of the HFF14Spo host galaxy are too faint in the GLASS data to provide any useful line identifications. There are also no other sources in the GLASS redshift catalog (<http://glass.astro.ucla.edu/>) that have a spectroscopic redshift consistent with $z = 1.0054$.

Gravitational Lens Models. The seven lens models used to provide estimates of the plausible range of magnifications and time delays are as follows:

- *CATS*: The model of [Ref. 10], version 4.1, generated with the LENSTOOL software (<http://projects.lam.fr/repos/lenstool/wiki>)⁶⁵ using strong lensing constraints. This model parameterizes cluster and galaxy components using pseudo-isothermal elliptical mass distribution (PIEMD) density profiles^{66,67}.
- *GLAFIC*: The model of [Ref. 68], built using the GLAFIC software (<http://www.slac.stanford.edu/~oguri/glafic/>)⁶⁹ with strong-lensing constraints. This model assumes simply parametrized mass distributions, and model parameters are constrained using positions of more than 100 multiple images.

- *GLEE*: A new model built using the *GLEE* software^{70,71} with the same strong-lensing constraints used in [Ref. 6], representing mass distributions with simply parameterized mass profiles.
- *GRALE*: A free-form, adaptive grid model developed using the *GRALE* software tool^{16,72–74}, which implements a genetic algorithm to reconstruct the cluster mass distribution with hundreds to thousands of projected Plummer⁷⁵ density profiles.
- *SWUnited*: The model of [Ref. 15], built using the *SWUnited* modeling method^{76,77}, in which an adaptive pixelated grid iteratively adapts the mass distribution to match both strong- and weak-lensing constraints. Time delay predictions are not available for this model.
- *WSLAP+*: Created with the *WSLAP+* software (<http://www.ifca.unican.es/users/jdiego/LensExplorer>)⁷⁸: Weak and Strong Lensing Analysis Package plus member galaxies (Note: no weak-lensing constraints were used for this MACS0416 model).
- *ZLTM*: A model with strong- and weak-lensing constraints, built using the “light-traces-mass” (LTM) methodology^{79,80}, first presented for MACS0416 in [Ref. 9].

Early versions of the *SWUnited*, *CATS*, *ZLTM* and *GRALE* models were originally distributed as part of the Hubble Frontier Fields lens modeling project (<https://archive.stsci.edu/prepds/frontier/lensmodels/>), in which models were generated based on data available before the start of the HFF observations to enable rapid early investigations of lensed sources. The versions of these models applied here are updated to incorporate additional lensing constraints. In all cases the lens modelers made use of strong-lensing constraints (multiply imaged systems and arcs) derived from *HST* imaging collected as part of the CLASH program⁵³). These models also made use of spectroscopic redshifts in the cluster field^{6,14,81,82}. Input weak-lensing constraints were derived from data collected at the Subaru Telescope by PI K. Umetsu (in prep) and archival imaging.

X-ray Nondetections. The MACS0416 field was observed by the *Swift* X-Ray Telescope and UltraViolet/Optical Telescope in April 2013. No source was detected near the locations of the HFF14Spo events (N. Gehrels, private communication). The field was also observed by *Chandra* with the ACIS-I instrument for three separate programs. On June 7, 2009 it was observed for GO program 10800770 (PI: H. Ebeling). It was revisited for GTO program 15800052 (PI: S. Murray) on November 20, 2013 and for GO program 15800858 (PI: C. Jones) on June 9, August 31, November 26, and December 17, 2014. These *Chandra* images show no evidence for an x-ray emitting point source near the HFF14Spo locations on those dates (S. Murray, private communication).

The *Chandra* observations that were closest in time to the observed HFF14Spo events were those taken in August and November, 2014. The August 31 observations were coincident with the observed peak of rest-frame optical emission for the HFF14Spo-SE event (on MJD 56900). The November 26 observations correspond to 44 rest-frame days after the peak of the HFF14Spo-SE

event. If the HFF14Spo events are UV/optical nova eruption, then these observations most likely did not coincide with the nova system’s supersoft x-ray phase. For a RN system the x-ray phase typically initiates after a short delay, and persists for a span of only a few weeks. For example, the most rapid recurrence nova known, M31N 2008-12a, has exhibited a supersoft x-ray phase from 6 to 18 days after the peak of the optical emission⁸³.

Light Curve Fitting. Due to the rapid decline timescale, no observations were collected for either event that unambiguously show the declining portion of the light curve. Therefore, we must make some assumptions for the shape of the light curve in order to quantify the peak luminosity and the corresponding timescales for the rise and the decline. We first approach this with a simplistic model that is piecewise linear in magnitude vs time. Supplementary Figure 3 shows examples of the resulting fits for the two events. For each fit we use only the data collected within 3 days of the brightest observed magnitude, which allows us to fit a linear rise separately for the F606W and F814W light curves for HFF14Spo-NW and the F125W and F160W light curves for HFF14Spo-SE. To quantify the covariance between the true peak brightness, the rise time and the decline timescale, we use the following procedure:

1. make an assumption for the date of peak, t_{pk} ;
2. measure the peak magnitude at t_{pk} from the linear fit to the rising light-curve data;
3. assume the source reaches a minimum brightness (maximum magnitude) of 30 AB mag at the epoch of first observation after the peak;
4. draw a line for the declining light curve between the assumed peak and the assumed minimum brightness;
5. use that declining light-curve line to measure the timescale for the event to drop by 2 mag, t_2 ;
6. make a new assumption for t_{pk} and repeat.

As shown in Supplementary Figure 3, the resulting piecewise linear fits are simplistic, but nevertheless approximately capture the observed behavior for both events. Furthermore, since this toy model is not physically motivated, it allows us to remain agnostic for the time being as to the astrophysical source(s) driving these transients. From these fits we can see that HFF14Spo-NW most likely reached a peak magnitude between 25 and 26.5 AB mag in both F814W and F435W, and had a decline timescale t_2 of less than 2 days in the rest frame. The observations of HFF14Spo-SE provide less stringent constraints, but we see that it had a peak magnitude between 23 and 26.5 AB mag in F160W and exhibited a decline time of less than seven days. These fits also illustrate the generic fact that a higher peak brightness corresponds to a longer rise time and a faster decline timescale, independent of the specific model used. Changes to the arbitrary constraints we placed on these linear fits do not substantially affect these results.

At any assumed value for the time of peak brightness this linear interpolation gives an estimate of the peak magnitude. We then convert that to a luminosity (e.g., νL_ν in erg s $^{-1}$) by first correcting for the luminosity distance assuming a standard Λ CDM cosmology, and then accounting for an assumed lensing magnification, μ . The range of plausible lensing magnifications ($10 < \mu < 100$) is derived from the union of our seven independent lens models. This results in a grid of possible peak luminosities for each event as a function of magnification and time of peak. As we are using linear light curve fits, the assumed time of peak is equivalent to an assumption for the decline time, which we quantify as t_2 , the time over which the transient declines by 2 magnitudes.

LBV Build-up Timescale and Quiescent Luminosity. To explore some of the physical implications of an LBV classification for the two HFF14Spo events, we first make a rough estimate of the total radiated energy, which can be computed using the decline timescale t_2 and the peak luminosity L_{pk} :

$$E_{\text{rad}} = \zeta t_2 L_{\text{pk}}, \quad (1)$$

where ζ is a dimensionless factor of order unity that depends on the precise shape of the light curve²⁹. Note that earlier work²⁹ has used $t_{1.5}$ instead of t_2 , which amounts to a different light-curve shape term, ζ . Adopting $L_{\text{pk}} \approx 10^{41}$ erg s $^{-1}$ and $t_2 \approx 1$ day (as shown in Fig. 5), we find that the total radiated energy is $E_{\text{rad}} \approx 10^{46}$ erg. A realistic range for this estimate would span $10^{44} < E_{\text{rad}} < 10^{47}$ erg, due to uncertainties in the magnification, bolometric luminosity correction, decline time, and light-curve shape. These uncertainties notwithstanding, our estimate falls well within the range of plausible values for the total radiated energy of a major LBV outburst.

The “build-up” timescale²⁹ matches the radiative energy released in an LBV eruption event with the radiative energy produced during the intervening quiescent phase,

$$t_{\text{rad}} = \frac{E_{\text{rad}}}{L_{\text{qui}}} = t_2 \frac{\zeta L_{\text{pk}}}{L_{\text{qui}}}, \quad (2)$$

where L_{qui} is the luminosity of the LBV progenitor star during quiescence.

The HFF14Spo events are not resolved as individual stars in their quiescent phase, so we have no useful constraint on the quiescent luminosity. Thus, instead of using a measured quiescent luminosity to estimate the build-up timescale, we assume that t_{rad} for HFF14Spo corresponds to the observed rest-frame lag between the two events, roughly 120 days (this accounts for both cosmic time dilation and a gravitational lensing time delay of ~ 40 days). Adopting $L_{\text{pk}} = 10^{41}$ erg s $^{-1}$ and $t_2 = 2$ days (see Figure 5), we infer that the quiescent luminosity of the HFF14Spo progenitor would be $L_{\text{qui}} \approx 10^{39.5}$ erg s $^{-1}$ ($M_V \approx -10$ mag).

RN Light-Curve Comparison. There are ten known RNe in the Milky Way galaxy, and seven of these exhibit outbursts that decline rapidly, fading by two magnitudes in less than ten days⁴⁰. Supplementary Figure 7 compares the HFF14Spo light curves to a composite light curve (the gray shaded region), which encompasses the V band light curve templates⁴⁰ for all seven of these galactic RN events. The Andromeda galaxy (M31) also hosts at least one RN with a rapidly declining light curve. The 2014 eruption of this well-studied nova, M31N 2008-12a, is shown as a solid black line in Supplementary Figure 7, fading by 2 mag in < 3 days. This comparison demonstrates that the rapid decline of both of the HFF14Spo transient events is fully consistent with the eruptions of known RNe in the local universe.

RN Luminosity and Recurrence Period. To examine the recurrence period and peak brightness of the HFF14Spo events relative to RNe, we rely on a pair of papers that evaluated an extensive grid of nova models through multiple cycles of outburst and quiescence^{46,84}. Supplementary Figure 8 plots first the RN outburst amplitude (the apparent magnitude between outbursts minus the apparent magnitude at peak) and then the peak luminosity against the log of the recurrence period in years. For the HFF14Spo events we can only measure a lower limit on the outburst amplitude, since the presumed progenitor star is unresolved, so no measurement is available at quiescence. Supplementary Figure 8 shows that a recurrence period as fast as one year is expected only for a RN system in which the primary white dwarf is both very close to the Chandrasekhar mass limit ($1.4 M_{\odot}$) and also has an extraordinarily rapid mass transfer rate ($\sim 10^{-6} M_{\odot} \text{ yr}^{-1}$). The models of [Ref. 46] suggest that such systems should have a very low peak amplitude (barely consistent with the lower limit for HFF14Spo) and a low peak luminosity (~ 100 times less luminous than the HFF14Spo events).

The closest analog for the HFF14Spo events from the population of known RN systems is the nova M31N 2008-12a. [Ref. 85] provided a theoretical model that can account for the key observational characteristics of this remarkable nova: the very rapid recurrence timescale (<1 yr), fast optical light curve ($t_2 \sim 2$ days), and short supersoft x-ray phase (6-18 days after optical outburst)⁸³. To match these observations, [Ref. 85] invoke a $1.38 M_{\odot}$ white dwarf primary, drawing mass from a companion at a rate of $1.6 \times 10^{-7} M_{\odot} \text{ yr}^{-1}$. This is largely consistent with the theoretical expectations derived by [Ref. 46], and reinforces the conclusion that a combination of a high-mass white dwarf and efficient mass transfer are the key ingredients for rapid recurrence and short light curves. The one feature that cannot be effectively explained with this hypothesis is the peculiarly high luminosity of the HFF14Spo events – even after accounting for the very large uncertainties.

Intracluster Light. To estimate the mass of intracluster stars along the line of sight to the HFF14Spo events, we follow the procedure of [Ref. 51] and Morishita et al. (in prep). This entails fitting and removing the surface brightness of individual galaxies in the field, then fitting a smooth profile to the residual surface brightness of intracluster light (ICL). The surface brightness is then converted to a projected stellar mass surface density by assuming a Chabrier⁸⁶ initial mass function and an exponentially declining star formation history. This procedure leads to an estimate for the intracluster stellar mass of $\log(\Sigma_{*}/(M_{\odot} \text{ kpc}^{-2})) = 6.9 \pm 0.4$. This is very similar to the value of $6.8^{+0.4}_{-0.3}$

inferred for the probable caustic crossing star M1149 LS1⁵¹.

Color Curves. At $z = 1$ the observed optical and infrared bands translate to rest-frame ultraviolet (UV) and optical wavelengths, respectively. To derive rest-frame UV and optical colors from the observed photometry, we start with the measured magnitude in a relatively blue band (F435W and F606W for HFF14Spo-NW and F105W, F125W, F140W for HFF14Spo-SE). We then subtract the coeval magnitude for a matched red band (F814W for HFF14Spo-NW, F125W or F160W for HFF14Spo-SE), derived from the linear fits to those bands. To adjust these to rest-frame filters, we apply K corrections⁸⁷, which we compute by defining a crude SED via linear interpolation between the observed broad bands for each transient event at each epoch. For consistency with past published results, we include in each K correction a transformation from AB to Vega-based magnitudes. The resulting UV and optical colors are plotted in Supplementary Figure 9. Both HFF14Spo-NW and HFF14Spo-SE show little or no color variation over the period where color information is available. This lack of color evolution is compatible with all three of the primary hypotheses advanced, as it is possible to have no discernible color evolution from either an LBV or RN over this short time span, and microlensing events inherently exhibit an unchanging color.

If these two events are from a single source then one could construct a composite SED from rest-frame UV to optical wavelengths by combining the NW and SE flux measurements, but only after correcting for the relative magnification. Figure 4 shows that the observed peak brightnesses for the two events agree to within $\sim 30\%$. This implies that for any composite SED, the rest-frame UV to optical flux ratio is approximately equal to the NW:SE magnification ratio, and any extreme asymmetry in the magnification would indicate a very steep slope in the SED.

Rates. To derive a rough estimate of the rate of HFF14Spo-like transients, we first define the set of strongly lensed galaxies in which a similarly faint and fast transient could have been detected in the HFF imaging. The single-epoch detection limit of the HFF transient search was $m_{\text{lim}} = 26.7$ AB mag, consistent with the SN searches carried out in the CLASH and CANDELS programs^{88,89}. For a transient with peak brightness $M_V > -14$ mag to be detected, the host galaxy must be amplified by strong lensing with a magnification $\mu > 20$ at $z \sim 1$, growing to $\mu > 100$ at $z \sim 2$. Using photometric redshifts and magnifications derived from the GLAFIC lens models of the six HFF clusters, we find $N_{\text{gal}} = 6$ galaxies that satisfy this criterion, with $0.5 < z < 1.5$ (Supplementary Figure 10).

We then define the *control time*, t_c , for the HFF survey, which gives the span of time over which each cluster was observed with a cadence sufficient for detection of such rapid transients. We define this as any period in which at least two *HST* observations were collected within every 10 day span. This effectively includes the entirety of the primary HFF campaigns on each cluster, but excludes all of the ancillary data collection periods from supplemental *HST* imaging programs. The average control time for an HFF cluster is $t_c = 0.22$ years (80 days). Treating each HFF14Spo event as a separate detection, we can derive a rate estimate using $R = 2/(N_{\text{gal}} t_c)$. This yields $R = 1.5$ events $\text{galaxy}^{-1} \text{ year}^{-1}$.

Future examination of the rate of such transients should consider the total stellar mass and the star-formation rates of the galaxies surveyed, or use a projection of the lensed background area onto the source plane to derive a volumetric rate. Such analyses would require a more detailed exploration of the impact of lensing uncertainties on derived properties of the lensed galaxies and the lensed volume, and this is beyond the scope of the current work.

References

1. Kasliwal, M. M. *et al.* Discovery of a New Photometric Sub-class of Faint and Fast Classical Novae. *ApJ* **735**, 94 (2011).
2. Drout, M. R. *et al.* Rapidly Evolving and Luminous Transients from Pan-STARRS1. *ApJ* **794**, 23 (2014).
3. Berger, E. *et al.* A Search for Fast Optical Transients in the Pan-STARRS1 Medium-Deep Survey: M-Dwarf Flares, Asteroids, Limits on Extragalactic Rates, and Implications for LSST. *ApJ* **779**, 18 (2013).
4. Tyson, J. A. Large Synoptic Survey Telescope: Overview. In Tyson, J. A. & Wolff, S. (eds.) *Survey and Other Telescope Technologies and Discoveries*, vol. 4836 of *Society of Photo-Optical Instrumentation Engineers (SPIE) Conference Series*, 10–20 (2002).
5. Lotz, J. M. *et al.* The Frontier Fields: Survey Design and Initial Results. *ApJ* **837**, 97 (2017).
6. Caminha, G. B. *et al.* A refined mass distribution of the cluster MACS J0416.1-2403 from a new large set of spectroscopic multiply lensed sources. *A&A* **600**, A90 (2017).
7. Pastorello, A. *et al.* Interacting Supernovae and Supernova Impostors: SN 2009ip, is this the End? *ApJ* **767**, 1 (2013).
8. Pastorello, A. *et al.* Multiple major outbursts from a restless luminous blue variable in NGC 3432. *MNRAS* **408**, 181–198 (2010).
9. Zitrin, A. *et al.* CLASH: The Enhanced Lensing Efficiency of the Highly Elongated Merging Cluster MACS J0416.1-2403. *ApJ* **762**, L30 (2013).
10. Jauzac, M. *et al.* Hubble Frontier Fields: a high-precision strong-lensing analysis of galaxy cluster MACSJ0416.1-2403 using 200 multiple images. *MNRAS* **443**, 1549–1554 (2014).
11. Johnson, T. L. *et al.* Lens Models and Magnification Maps of the Six Hubble Frontier Fields Clusters. *ApJ* **797**, 48 (2014).
12. Richard, J. *et al.* Mass and magnification maps for the Hubble Space Telescope Frontier Fields clusters: implications for high-redshift studies. *MNRAS* **444**, 268–289 (2014).
13. Diego, J. M. *et al.* A free-form lensing grid solution for A1689 with new multiple images. *MNRAS* **446**, 683–704 (2015).

14. Grillo, C. *et al.* CLASH-VLT: Insights on the Mass Substructures in the Frontier Fields Cluster MACS J0416.1-2403 through Accurate Strong Lens Modeling. *ApJ* **800**, 38 (2015).
15. Hoag, A. *et al.* The Grism Lens-Amplified Survey from Space (GLASS). VI. Comparing the Mass and Light in MACS J0416.1-2403 Using Frontier Field Imaging and GLASS Spectroscopy. *ApJ* **831**, 182 (2016).
16. Sebesta, K., Williams, L. L. R., Mohammed, I., Saha, P. & Liesenborgs, J. Testing light-traces-mass in Hubble Frontier Fields Cluster MACS-J0416.1-2403. *MNRAS* **461**, 2126–2134 (2016).
17. Karoff, C. *et al.* Observational evidence for enhanced magnetic activity of superflare stars. *Nature Communications* **7**, 11058 (2016).
18. Kulkarni, S. R. *et al.* An unusually brilliant transient in the galaxy M85. *Nature* **447**, 458–460 (2007).
19. Gal-Yam, A. Luminous Supernovae. *Science* **337**, 927– (2012).
20. Foley, R. J. *et al.* Type Iax Supernovae: A New Class of Stellar Explosion. *ApJ* **767**, 57 (2013).
21. Kasliwal, M. M. *et al.* Calcium-rich Gap Transients in the Remote Outskirts of Galaxies. *ApJ* **755**, 161 (2012).
22. Li, L.-X. & Paczyński, B. Transient Events from Neutron Star Mergers. *ApJ* **507**, L59–L62 (1998).
23. Warner, B. The AM Canum Venaticorum Stars. *Ap&SS* **225**, 249–270 (1995).
24. Bildsten, L., Shen, K. J., Weinberg, N. N. & Nelemans, G. Faint Thermonuclear Supernovae from AM Canum Venaticorum Binaries. *ApJ* **662**, L95–L98 (2007).
25. Metzger, B. D. *et al.* Electromagnetic counterparts of compact object mergers powered by the radioactive decay of r-process nuclei. *MNRAS* **406**, 2650–2662 (2010).
26. Barnes, J. & Kasen, D. Effect of a High Opacity on the Light Curves of Radioactively Powered Transients from Compact Object Mergers. *ApJ* **775**, 18 (2013).
27. Kasen, D., Fernández, R. & Metzger, B. D. Kilonova light curves from the disc wind outflows of compact object mergers. *MNRAS* **450**, 1777–1786 (2015).
28. Shen, K. J., Kasen, D., Weinberg, N. N., Bildsten, L. & Scannapieco, E. Thermonuclear Ia Supernovae from Helium Shell Detonations: Explosion Models and Observables. *ApJ* **715**, 767–774 (2010).

29. Smith, N., Li, W., Silverman, J. M., Ganeshalingam, M. & Filippenko, A. V. Luminous blue variable eruptions and related transients: diversity of progenitors and outburst properties. *MNRAS* **415**, 773–810 (2011).
30. Kochanek, C. S., Szczygieł, D. M. & Stanek, K. Z. Unmasking the Supernova Impostors. *ApJ* **758**, 142 (2012).
31. Maza, J. *et al.* Supernova 2009ip in ngc 7259. *CBET* 1 (2009).
32. Miller, A. A. *et al.* A Previous Transient Consistent with the Location of SN 2009ip Suggests that SN 2009ip is Not a Supernova. *The Astronomer's Telegram* **2183** (2009).
33. Li, W., Smith, N., Miller, A. A. & Filippenko, A. V. Rebrightening of SN 2009ip is Reminiscent of eta Carinae Just Before 1843 Eruption. *The Astronomer's Telegram* **2212** (2009).
34. Berger, E., Foley, R. & Ivans, I. SN 2009ip is an LBV Outburst. *The Astronomer's Telegram* **2184** (2009).
35. Kilpatrick, C. D. *et al.* Connecting the progenitors, pre-explosion variability, and giant outbursts of luminous blue variables with Gaia16cfr. *arXiv: 1706.09962* (2017).
36. Pastorello, A. *et al.* Supernovae 2016bdu and 2005gl, and their link with SN 2009ip-like transients: another piece of the puzzle. *arXiv: 1707.00611* (2017).
37. Della Valle, M. & Livio, M. The Calibration of Novae as Distance Indicators. *ApJ* **452**, 704 (1995).
38. Downes, R. A. & Duerbeck, H. W. Optical Imaging of Nova Shells and the Maximum Magnitude-Rate of Decline Relationship. *AJ* **120**, 2007–2037 (2000).
39. Shafter, A. W. *et al.* A Spectroscopic and Photometric Survey of Novae in M31. *ApJ* **734**, 12 (2011).
40. Schaefer, B. E. Comprehensive Photometric Histories of All Known Galactic Recurrent Novae. *ApJS* **187**, 275–373 (2010).
41. Tang, S. *et al.* An Accreting White Dwarf near the Chandrasekhar Limit in the Andromeda Galaxy. *ApJ* **786**, 61 (2014).
42. Darnley, M. J. *et al.* A remarkable recurrent nova in M 31: The optical observations. *A&A* **563**, L9 (2014).
43. Darnley, M. J. *et al.* A remarkable recurrent nova in M31: Discovery and optical/UV observations of the predicted 2014 eruption. *A&A* **580**, A45 (2015).
44. Henze, M. *et al.* A remarkable recurrent nova in M 31: The 2010 eruption recovered and evidence of a six-month period. *A&A* **582**, L8 (2015).

45. Darnley, M. J. *et al.* M31N 2008-12a - The Remarkable Recurrent Nova in M31: Panchromatic Observations of the 2015 Eruption. *ApJ* **833**, 149 (2016).
46. Yaron, O., Prialnik, D., Shara, M. M. & Kovetz, A. An Extended Grid of Nova Models. II. The Parameter Space of Nova Outbursts. *ApJ* **623**, 398–410 (2005).
47. Schneider, P. & Weiss, A. The two-point-mass lens - Detailed investigation of a special asymmetric gravitational lens. *A&A* **164**, 237–259 (1986).
48. MiraldaEscude, J. The magnification of stars crossing a caustic. I - Lenses with smooth potentials. *ApJ* **379**, 94–98 (1991).
49. Lewis, G. F., Miralda-Escude, J., Richardson, D. C. & Wambsganss, J. Microlensing light curves - A new and efficient numerical method. *MNRAS* **261**, 647–656 (1993).
50. Diego, J. M. *et al.* Dark matter under the microscope: Constraining compact dark matter with caustic crossing events. *arXiv:1706.10281* (2017).
51. Kelly, P. L. *et al.* An individual star at redshift 1.5 extremely magnified by a galaxy-cluster lens. *arXiv:1706.10279* (2017).
52. Rodney, S. A. *et al.* Illuminating a Dark Lens : A Type Ia Supernova Magnified by the Frontier Fields Galaxy Cluster Abell 2744. *ApJ* **811**, 70 (2015).
53. Postman, M. *et al.* The Cluster Lensing and Supernova Survey with Hubble: An Overview. *ApJS* **199**, 25 (2012).
54. Jones, D. O., Scolnic, D. M. & Rodney, S. A. PythonPhot: Simple DAOPHOT-type photometry in Python. *Astrophysics Source Code Library* (2015).
55. Vernet, J. *et al.* X-shooter, the new wide band intermediate resolution spectrograph at the ESO Very Large Telescope. *A&A* **536**, A105 (2011).
56. Benítez, N. Bayesian Photometric Redshift Estimation. *ApJ* **536**, 571–583 (2000).
57. Brammer, G. B., van Dokkum, P. G. & Coppi, P. EAZY: A Fast, Public Photometric Redshift Code. *ApJ* **686**, 1503–1513 (2008).
58. Le Fèvre, O. *et al.* Commissioning and performances of the VLT-VIMOS instrument. In Iye, M. & Moorwood, A. F. M. (eds.) *Instrument Design and Performance for Optical/Infrared Ground-based Telescopes*, vol. 4841 of *Society of Photo-Optical Instrumentation Engineers (SPIE) Conference Series*, 1670–1681 (2003).
59. Rosati, P. *et al.* CLASH-VLT: A VIMOS Large Programme to Map the Dark Matter Mass Distribution in Galaxy Clusters and Probe Distant Lensed Galaxies. *The Messenger* **158**, 48–53 (2014).

60. Balestra, I. *et al.* CLASH-VLT: Dissecting the Frontier Fields Galaxy Cluster MACS J0416.1-2403 with 800 Spectra of Member Galaxies. *ApJS* **224**, 33 (2016).
61. Henault, F. *et al.* MUSE: a second-generation integral-field spectrograph for the VLT. In Iye, M. & Moorwood, A. F. M. (eds.) *Instrument Design and Performance for Optical/Infrared Ground-based Telescopes*, vol. 4841 of Proc. SPIE, 1096–1107 (2003).
62. Bacon, R. *et al.* News of the MUSE. *The Messenger* **147**, 4–6 (2012).
63. Schmidt, K. B. *et al.* Through the Looking GLASS: HST Spectroscopy of Faint Galaxies Lensed by the Frontier Fields Cluster MACSJ0717.5+3745. *ApJ* **782**, L36 (2014).
64. Treu, T. *et al.* The Grism Lens-Amplified Survey from Space (GLASS). I. Survey Overview and First Data Release. *ApJ* **812**, 114 (2015).
65. Jullo, E. *et al.* A Bayesian approach to strong lensing modelling of galaxy clusters. *New Journal of Physics* **9**, 447 (2007).
66. Kassiola, A. & Kovner, I. Elliptic Mass Distributions versus Elliptic Potentials in Gravitational Lenses. *ApJ* **417**, 450 (1993).
67. Limousin, M. *et al.* Combining Strong and Weak Gravitational Lensing in Abell 1689. *ApJ* **668**, 643–666 (2007).
68. Kawamata, R., Oguri, M., Ishigaki, M., Shimasaku, K. & Ouchi, M. Precise Strong Lensing Mass Modeling of Four Hubble Frontier Field Clusters and a Sample of Magnified High-redshift Galaxies. *ApJ* **819**, 114 (2016).
69. Oguri, M. The Mass Distribution of SDSS J1004+4112 Revisited. *PASJ* **62**, 1017– (2010).
70. Suyu, S. H. & Halkola, A. The halos of satellite galaxies: the companion of the massive elliptical lens SL2S J08544-0121. *A&A* **524**, A94 (2010).
71. Suyu, S. H. *et al.* Disentangling Baryons and Dark Matter in the Spiral Gravitational Lens B1933+503. *ApJ* **750**, 10 (2012).
72. Liesenborgs, J., De Rijcke, S. & Dejonghe, H. A genetic algorithm for the non-parametric inversion of strong lensing systems. *MNRAS* **367**, 1209–1216 (2006).
73. Liesenborgs, J., de Rijcke, S., Dejonghe, H. & Bekaert, P. Non-parametric inversion of gravitational lensing systems with few images using a multi-objective genetic algorithm. *MNRAS* **380**, 1729–1736 (2007).
74. Mohammed, I., Liesenborgs, J., Saha, P. & Williams, L. L. R. Mass-galaxy offsets in Abell 3827, 2218 and 1689: intrinsic properties or line-of-sight substructures? *MNRAS* **439**, 2651–2661 (2014).

75. Plummer, H. C. On the problem of distribution in globular star clusters. *MNRAS* **71**, 460–470 (1911).
76. Bradač, M., Schneider, P., Lombardi, M. & Erben, T. Strong and weak lensing united. *A&A* **437**, 39–48 (2005).
77. Bradač, M. *et al.* Focusing Cosmic Telescopes: Exploring Redshift $z \sim 5\text{--}6$ Galaxies with the Bullet Cluster 1E0657 - 56. *ApJ* **706**, 1201–1212 (2009).
78. Sendra, I., Diego, J. M., Broadhurst, T. & Lazkoz, R. Enabling non-parametric strong lensing models to derive reliable cluster mass distributions - WSLAP+. *MNRAS* **437**, 2642–2651 (2014).
79. Zitrin, A. *et al.* New multiply-lensed galaxies identified in ACS/NIC3 observations of Cl0024+1654 using an improved mass model. *MNRAS* **396**, 1985–2002 (2009).
80. Zitrin, A. *et al.* Hubble Space Telescope Combined Strong and Weak Lensing Analysis of the CLASH Sample: Mass and Magnification Models and Systematic Uncertainties. *ApJ* **801**, 44 (2015).
81. Mann, A. W. & Ebeling, H. X-ray-optical classification of cluster mergers and the evolution of the cluster merger fraction. *MNRAS* **420**, 2120–2138 (2012).
82. Christensen, L. *et al.* The low-mass end of the fundamental relation for gravitationally lensed star-forming galaxies at $1 \leq z \leq 6$. *MNRAS* **427**, 1953–1972 (2012).
83. Henze, M. *et al.* A remarkable recurrent nova in M 31: The predicted 2014 outburst in X-rays with Swift. *A&A* **580**, A46 (2015).
84. Prialnik, D. & Kovetz, A. An extended grid of multicycle nova evolution models. *ApJ* **445**, 789–810 (1995).
85. Kato, M., Saio, H. & Hachisu, I. Multi-wavelength Light Curve Model of the One-year Recurrence Period Nova M31N 2008-12A. *ApJ* **808**, 52 (2015).
86. Chabrier, G. Galactic Stellar and Substellar Initial Mass Function. *PASP* **115**, 763–795 (2003).
87. Hogg, D. W., Baldry, I. K., Blanton, M. R. & Eisenstein, D. J. The k correction. *arXiv:astro-ph/0210394* (2002).
88. Graur, O. *et al.* Type-Ia Supernova Rates to Redshift 2.4 from CLASH: The Cluster Lensing And Supernova Survey with Hubble. *ApJ* **783**, 28 (2014).
89. Rodney, S. A. *et al.* Type Ia Supernova Rate Measurements to Redshift 2.5 from CANDELS: Searching for Prompt Explosions in the Early Universe. *AJ* **148**, 13 (2014).

90. Sérsic, J. L. Influence of the atmospheric and instrumental dispersion on the brightness distribution in a galaxy. *Boletin de la Asociacion Argentina de Astronomia La Plata Argentina* **6**, 41 (1963).
91. Akaike, H. A new look at the statistical model identification. *Automatic Control, IEEE Transactions on* **19**, 716–723 (1974).
92. Hemmati, S. *et al.* Kiloparsec-scale Properties of Emission-line Galaxies. *ApJ* **797**, 108 (2014).
93. Wambsganss, J. Quasar Microlensing. In Brainerd, T. G. & Kochanek, C. S. (eds.) *Gravitational Lensing: Recent Progress and Future Go*, vol. 237 of *Astronomical Society of the Pacific Conference Series*, 185 (2001).
94. Kochanek, C. S. Quantitative Interpretation of Quasar Microlensing Light Curves. *ApJ* **605**, 58–77 (2004).
95. Paczynski, B. Gravitational microlensing by the galactic halo. *ApJ* **304**, 1–5 (1986).
96. Alcock, C. *et al.* Possible gravitational microlensing of a star in the Large Magellanic Cloud. *Nature* **365**, 621–623 (1993).
97. Aubourg, E. *et al.* Evidence for gravitational microlensing by dark objects in the Galactic halo. *Nature* **365**, 623–625 (1993).
98. Udalski, A. *et al.* The optical gravitational lensing experiment. Discovery of the first candidate microlensing event in the direction of the Galactic Bulge. *ACTAA* **43**, 289–294 (1993).
99. Chang, K. & Refsdal, S. Flux variations of QSO 0957+561 A, B and image splitting by stars near the light path. *Nature* **282**, 561–564 (1979).
100. Chang, K. & Refsdal, S. Star disturbances in gravitational lens galaxies. *A&A* **132**, 168–178 (1984).
101. Planck Collaboration *et al.* Planck 2015 results. XIII. Cosmological parameters. *A&A* **594**, A13 (2016).

Supplementary Information Supplementary figures, tables and notes are included at the end of this document.

Acknowledgements The authors thank Mario Livio and Laura Chomiuk for helpful discussion of this paper, as well as Stephen Murray and Neil Gehrels for assistance with the *Chandra* and *Swift* data, respectively. Financial support for this work was provided to S.A.R., O.G., and L.G.S. by NASA through grant HST-GO-13386 from the Space Telescope Science Institute (STScI), which is operated by Associated Universities for Research in Astronomy, Inc. (AURA), under NASA contract NAS 5-26555. J.M.D acknowledges support of the projects AYA2015-64508-P (MINECO/FEDER, UE), AYA2012-39475-C02-01 and the consolider

project CSD2010-00064 funded by the Ministerio de Economia y Competitividad. A.V.F. and P.L.K. are grateful for financial assistance from the Christopher R. Redlich Fund, the TABASGO Foundation, and NASA/STScI grants 14528, 14872, and 14922. The work of A.V.F. was conducted in part at the Aspen Center for Physics, which is supported by NSF grant PHY-1607611; he thanks the Center for its hospitality during the neutron stars workshop in June and July 2017. R.J.F. and the UCSC group is supported in part by NSF grant AST-1518052 and from fellowships from the Alfred P. Sloan Foundation and the David and Lucile Packard Foundation to R.J.F. C.G. acknowledges support by VILLUM FONDEN Young Investigator Programme through grant no. 10123. M.J. was supported by the Science and Technology Facilities Council (grant number ST/L00075X/1) and used the DiRAC Data Centric system at Durham University, operated by the Institute for Computational Cosmology on behalf of the STFC DiRAC HPC Facility (www.dirac.ac.uk). M.J. was funded by BIS National E-infrastructure capital grant ST/K00042X/1, STFC capital grant ST/H008519/1, and STFC DiRAC Operations grant ST/K003267/1 and Durham University. DiRAC is part of the National E-Infrastructure. R.K. was supported by Grant-in-Aid for JSPS Research Fellow (16J01302). M.O. acknowledges support in part by World Premier International Research Center Initiative (WPI Initiative), MEXT, Japan, and JSPS KAKENHI Grant Number 26800093 and 15H05892. J.R. acknowledges support from the ERC starting grant 336736-CALENDS. G.C. and S.H.S. thank the Max Planck Society for support through the Max Planck Research Group of S.H.S. T.T. and the GLASS team were funded by NASA through HST grant HST-GO-13459 from STScI. L.L.R.W. would like to thank Minnesota Supercomputing Institute at the University of Minnesota for providing resources and support.

Correspondence Correspondence and requests for materials should be addressed to S.A.R. (email: srodney@sc.edu).

Supplementary Information

Lens Model Variations. Supplementary Figure 1 presents probability distributions for the three magnifications and two time delay values of interest. These distributions were derived by combining the Monte Carlo chains from the CATS, GLAFIC, GLEE, and ZLTM models, and individual runs of the GRALE model, which uses a different random seed for each run. We applied a weight to each model to account for the different number of model iterations used by each modeling team. All five of these models agree that host image 11.3 is the leading image, appearing some 3–7 years before the other two images. The models do not agree on the arrival sequence of images 11.1 and 11.2: some have the NW image 11.2 as a leading image, and others have it as a trailing image. However, the models do consistently predict that the separation in time between those two images should be roughly in the range of 1 to 60 days.

Because of the proximity of the critical curves in all models, the predicted time delays and magnification factors are significantly different if calculated at the model-predicted positions instead of the observed positions. For example, in the GLEE model series (GLEE and GLEE-var) when switching from the observed to model-predicted positions the arrival order of the NW and SE images flips, the expected time delay drops from tens of days to <1 day, and the magnifications change by 30–60%. However, the expected magnifications and time delays between the events still fall within the broad ranges summarized in Table 1 and shown in Supplementary Figure 1. Regardless of whether the model predictions are extracted at the observed or predicted positions of the HFF14Spo events, none of the lens models can accommodate the observed 234-day time difference as purely a gravitational lensing time delay.

We used variations of several lens models to investigate how the lensing critical curves shift under a range of alternative assumptions or input constraints. These variations highlight the range of systematic effects that might impact the model predictions for the HFF14Spo magnifications, time delays and proximity to the critical curves. Figure 3 shows the critical curves for a source at $z = 1$ (the redshift of the HFF14Spo host galaxy) predicted by our seven baseline models, plus the four variations described below. Within a given model, variations that move a critical curve closer to the position of HFF14Spo-NW would drive the magnification of that event much higher (toward $\mu_{\text{NW}} \approx 200$). This generally also has the effect of moving the critical curve farther from HFF14Spo-SE, which would necessarily drive its magnification downward (toward $\mu_{\text{SE}} \approx 10$).

The baseline CATS model reported in Table 1 corresponds to the CATSv4.1 model published on the STScI Frontier Fields lens model repository (<https://archive.stsci.edu/pub/hlsp/frontier/macs0416/models/cats/v4.1/>). That model uses 178 cluster member galaxies, including a galaxy $< 5''$ south of the HFF14Spo host galaxy, which creates a local critical curve that intersects the HFF14Spo-SE location. Our CATS-var model is an earlier iteration of the model, published on the STScI repository as CATSv4 (<https://archive.stsci.edu/pub/hlsp/frontier/macs0416/models/cats/v4/>), and includes only 98 galaxies identified as cluster members. In this variation the nearby cluster member galaxy is not included, so the HFF14Spo-SE event is not intersected by a critical curve. However, the

HFF14Spo-NW event is approximately coincident with the primary critical curve of the MACS0416 cluster. When the critical curve is close to either HFF14Spo location, the magnifications predicted by the CATS model are driven up to $\mu > 100$. However, the time delays remain small, on the order of tens of days, and incompatible with the observed 234-day gap.

The WSLAP-var model evaluates whether the cluster redshift significantly impacts the positioning of the critical curve. In this merging cluster, the northern brightest cluster galaxy (BCG) has a slighter higher redshift than the southern BCG. The mean redshift of the cluster is not precisely determined, since it is likely to be aligned somewhat along the line of sight. For the WSLAP-var model we shift the assumed cluster redshift $z = 0.4$ from the default $z = 0.396$ (used in all the baseline models). The shift in the critical curve is noticeable, but not substantial, insofar as this change does not drive the critical curve to intersect either or both of the HFF14Spo locations.

The GLEE-var model is a multi-plane lens model (Chirivì et al., in prep.) that incorporates 13 galaxies with spectroscopic redshifts that place them either in the foreground or background of the MACS0416 cluster. Supplementary Figure 2 marks these 13 galaxies and highlights two of them that appear in the foreground of the HFF14Spo host galaxy and are close to the lines of sight to the HFF14Spo transients. Both the foreground $z = 0.0557$ galaxy and the reconstructed position of the $z = 0.9397$ galaxy have a projected separation of $<4''$ from the HFF14Spo-SE transient position. Including these galaxies in the GLEE lensing model changes the absolute value of the magnifications at the location of HFF14Spo-NW (HFF14Spo-SE) to ~ 70 (~ 250) and the time delay between the two locations to ~ 50 days. The line-of-sight galaxies also result in a shift of the position of the critical curve—as can be seen by comparing the GLEE and GLEE-var models in Figure 3. Nonetheless, the predicted time delays are still incompatible with the observed gap of 234 days between events.

The GLAFIC-var model examines whether it is plausible for a critical curve to intersect both HFF14Spo locations—contrary to the baseline assumption of a single critical curve subtending the HFF14Spo host galaxy roughly midway between the two positions. This model includes a customized constraint, requiring that the magnification factors at the HFF14Spo positons are > 1000 . To achieve this, we independently adjusted the mass scaling for the two nearest cluster member galaxies, which are located just northeast and south of the HFF14Spo host galaxy arc. The mass of the northeast member galaxy was increased by $\sim 30\%$ and that of the southern one by $\sim 60\%$. As a simple check of the predicted morphology of the host galaxy, we placed a source with a simple Sersic profile⁹⁰ on the source plane. The lensed image of that artificial source is an unbroken elongated arc, reproducing the host galaxy image morphology reasonably well.

For this modification of the GLAFIC lens model to be justified in a statistical sense, the revised model should still accurately reproduce the observed strong-lensing constraints across the entire cluster. The χ^2 statistic for the baseline GLAFIC model is 240, with 196 degrees of freedom ($\chi^2_\nu = 1.2$), and yields an Akaike information criterion (AIC)⁹¹ of 676. For the GLAFIC-var model that forces multiple critical curves to intersect the HFF14Spo locations, we get $\chi^2=331$ for 192 degrees of freedom ($\chi^2_\nu = 1.7$) and AIC=769. This suggests that the multiple critical curve

GLAFIC-var model is strongly disfavored by the *positional* strong-lensing constraints that are used for both models. However, we note that neither model incorporates the temporal constraints of the observed time delay.

A second variation of the CATS model (CATS-var2) was also used to test the plausibility of multiple critical curves intersecting the HFF14Spo locations. As in the GLAFIC-var case, this model requires that critical curves pass very near the HFF14Spo positions. The model can accommodate that constraint, insofar as the root mean square (RMS) error of the best-fit model is similar to that of the CATS and CATS-var models. However, in this CATS-var2 model the HFF14Spo host galaxy is predicted to be multiply-imaged 5 times. The *HST* images do not exhibit any breaks or substructure in the arc that would be generally expected in such a situation.

Moreover, this CATS-var2 model has strong implications for a separate background galaxy in the vicinity of image 11.3 (system 14 in [Ref. 6]). This galaxy is strongly lensed by a pair of spectroscopically confirmed cluster member galaxies⁶. Comparing the observed positions of the multiple images of System 14 against the CATS-var2 model-predicted positions, we find that this System contributes significantly to the global RMS error for the model—indicating that the CATS-var2 model can not accurately reproduce the multiple images of System 14. Conversely, when this system is removed as a model constraint, the RMS error decreases, and the CATS-var2 model can more successfully pass the critical line through the two HFF14Spo locations. A possible interpretation of this is that the established strong lensing constraints (especially System 14) are incompatible with the requirement that multiple critical curves must intersect the two HFF14Spo locations.

Host Galaxy To examine whether the two transients originated from the same physical location in the source plane, we looked for differences in the properties of the HFF14Spo host galaxy at the location of each event. We first used the technique of “pixel-by-pixel” SED fitting⁹² to determine rest-frame colors and stellar properties in a single resolution element of the *HST* imaging data. For this purpose we used the deepest possible stacks of *HST* images, comprising all available data except those images where the transient events were present. The resulting maps of stellar population properties are shown in Supplementary Figure 4. Supplementary Table 2 reports measurements of the three derived stellar population properties (color, mass, age) from host images 11.1, 11.2 and 11.3. In 11.1 and 11.2 these measurements were extracted from the central pixel at the location of each of the two HFF14Spo events. The lensing magnification here ranges from $\mu = 10$ to 200, corresponding to a size on the source plane between 6 and 600 pc². For host image 11.3 we report the stellar population properties derived from the pixel at the center of the galaxy, because the lens models do not have sufficient precision to map the HFF14Spo locations to specific positions in image 11.3. With a magnification of ~ 3 to 5, this extraction region covers roughly 2000 to 6000 pc².

The reported uncertainties for these derived stellar properties in Table 2 reflect only the measurement errors from the SED fitting, and do not attempt to quantify potential systematic biases. Such biases could arise, for example, from color differences in the background light, which

Supplementary Table 1: Measurements of the [OII] $\lambda\lambda 3626, 3629$ lines from HFF14Spo host galaxy images 11.1 and 11.2

Aperture ID	R.A. J2000 (degrees)	Dec. J2000 (degrees)	distance to HFF14Spo-SE (Arcsec)	[OII] Flux ($\text{erg s}^{-1} \text{cm}^{-2}$)	λ_{center} (Å)	FWHM (Å)	[OII] Flux ($\text{erg s}^{-1} \text{cm}^{-2}$)	λ_{center} (Å)	FWHM (Å)	Line Ratio
1	64.039371	-24.070450	-1.54	2.19e-18	7472.37	4.00	3.57e-18	7478.17	4.00	1.63
2	64.039218	-24.070345	-0.88	4.73e-18	7472.16	4.00	5.30e-18	7478.12	3.40	1.12
3	64.039078	-24.070264	-0.30	5.05e-18	7472.29	4.00	6.10e-18	7478.27	3.73	1.21
4	64.038921	-24.070163	0.39	4.22e-18	7472.19	4.00	5.74e-18	7478.08	3.59	1.36
5	64.038785	-24.070078	0.97	3.86e-18	7472.25	4.00	6.56e-18	7478.19	4.00	1.70
6	64.038637	-24.069958	1.65	4.80e-18	7472.51	4.00	5.42e-18	7478.07	2.69	1.13
7	64.038501	-24.069865	2.24	4.60e-18	7472.57	3.43	5.74e-18	7478.17	3.20	1.25
8	64.038352	-24.069752	2.92	4.70e-18	7472.54	3.54	6.22e-18	7478.16	2.95	1.32
9	64.038229	-24.069648	3.50	3.26e-18	7472.83	2.80	5.79e-18	7478.16	2.84	1.77
10	64.038076	-24.069532	4.19	2.44e-18	7473.01	2.57	3.22e-18	7478.10	2.73	1.32
NW	64.038565	-24.069939	1.90	4.30e-18	7472.55	3.13	5.49e-18	7478.01	2.89	1.28
SE	64.038998	-24.070241	0.00	4.37e-18	7472.46	4.00	6.10e-18	7478.22	3.79	1.40

is dominated by the cluster galaxies and varies significantly across the MACS0416 field. Such a bias might shift the absolute values of the parameter scales for any given host image (e.g., making the galaxy as a whole appear bluer, more massive, and younger). However, the gradients across any single host image are unlikely to be driven primarily by such systematics.

Supplementary Figure 4 and Supplementary Table 2 show that the measured values of the color, stellar mass, and age at the two HFF14Spo locations are mutually consistent. Thus, it is plausible to assume that the two positions map back to the same physical location at the source plane. Comparing those two locations to the center of the galaxy as defined in image 11.3, we see only a mild tension in the rest frame $U - V$ color. This comparison therefore cannot quantitatively rule out the possibility that the two transient events are located at the center of the galaxy. However, the maps shown in Supplementary Figure 4 do show a gradient in both $U - V$ color and stellar age. For both images 11.1 and 11.2 the bluest and youngest stars ($U - V \approx 0.3$, $\tau \approx 280$ Myr) are localized in knots near the extreme ends of each image, well separated from either of the HFF14Spo transient events. In the less distorted host image 11.3 the bluer and younger stars are concentrated near the center. Taken together, these color and age gradients suggest that the two transients are not coincident with the center of their host galaxy.

In addition to the *HST* imaging data, we also have spatially resolved spectroscopy from the MUSE integral field data. The only significant spectral line feature for the HFF14Spo host is the [OII] $\lambda\lambda 3726, 3729$ doublet, observed at 7474 and 7478 Å. To examine this feature in detail, one-dimensional spectra were extracted from the three-dimensional MUSE data cube at a series of locations along the HFF14Spo host-galaxy arc.

Supplementary Figure 5 depicts the apertures used for these extractions, shows the observed [OII] lines at the HFF14Spo-NW and SE positions, and compares the [OII] line profiles to other positions along the length of the host-galaxy arc. At each position the lines were extracted using

apertures with a radius of 0.6'', so adjacent extractions are not independent, although the two extractions centered on the HFF14Spo-NW and -SE positions have no overlap.

A difference in the shape of the [OII] lines or the doublet line ratio could provide evidence for a different environment at the two HFF14Spo locations, which would suggest that the two events emerged from independent sources. For a visual test for spectral deviations, we first constructed a mean spectrum by averaging the 1-D spectra from five non-overlapping apertures (apertures 1, 3, 5, 7, 9). To account for differences in magnification and host-galaxy intensity across the arc, each input spectrum was normalized at the wavelength 7477.7 Å, which corresponds to the center of the λ 3729 component of the [OII] emission line. This mean spectrum was then subtracted from the 1-D spectrum of each aperture, producing a set of “residual spectra,” shown in Supplementary Figure 5 in the lower-left panel. These spectra show no indication of a systematic trend in the wavelength position, shape or line ratio across the arc. Similarly, a comparison of the spectra from the HFF14Spo-NW and SE locations (right panels of Supplementary Figure 5) reveals no significant difference in the [OII] line shapes.

This qualitative comparison is borne out by a more quantitative assessment, reported in Table 1. We fit a Gaussian profile to each component of the [OII] doublet, separately in each extracted 1-D spectrum. From these fits we measured the integrated line flux, observed wavelength of line center (λ_{center}), full width at half maximum intensity (FWHM), and the intensity ratio of the two components of the doublet. These quantities—all reported in Table 1—do not exhibit any discernible gradient across the host galaxy. Thus, the [OII] measurements from MUSE cannot be used to distinguish either HFF14Spo location from the other, or to definitively answer whether either position is coincident with the center of the host galaxy (as would be required, for example, if these transients were from an AGN). We conclude that it is entirely plausible but not certain that the two HFF14Spo events arose from the same physical location in the host galaxy.

LBV Light-Curve Comparison. Supplementary Figure 6 presents a direct comparison of the observed HFF14Spo light curves against the light curves of the two LBVs that have well-studied rapid eruptions: SN 2009ip and NGC3432-LBV1. The brief outbursts of these LBVs have been less finely sampled than the two HFF14Spo events, but the available data show a wide variety of rise and decline times, even for a single object over a relatively narrow time window of a few months.

RN Light-Curve Comparison. There are ten known RNe in the Milky Way galaxy, and seven of these exhibit outbursts that decline rapidly, fading by two magnitudes in less than ten days⁴⁰. Supplementary Figure 7 compares the HFF14Spo light curves to a composite light curve (the gray shaded region), which encompasses the V band light curve templates⁴⁰ for all seven of these galactic RN events. The Andromeda galaxy (M31) also hosts at least one RN with a rapidly declining light curve. The 2014 eruption of this well-studied nova, M31N 2008-12a, is shown as a solid black line in Supplementary Figure 7, fading by 2 mag in < 3 days. This comparison demonstrates that the rapid decline of both of the HFF14Spo transient events is fully consistent with the eruptions of known RNe in the local universe.

RN Luminosity and Recurrence Period. To examine the recurrence period and peak brightness of the HFF14Spo events relative to RNe, we rely on a pair of papers that evaluated an extensive grid of nova models through multiple cycles of outburst and quiescence^{46,84}. Supplementary Figure 8 plots first the RN outburst amplitude (the apparent magnitude between outbursts minus the apparent magnitude at peak) and then the peak luminosity against the log of the recurrence period in years. For the HFF14Spo events we can only measure a lower limit on the outburst amplitude, since the presumed progenitor star is unresolved, so no measurement is available at quiescence. Supplementary Figure 8 shows that a recurrence period as fast as one year is expected only for a RN system in which the primary white dwarf is both very close to the Chandrasekhar mass limit ($1.4 M_{\odot}$) and also has an extraordinarily rapid mass transfer rate ($\sim 10^{-6} M_{\odot} \text{ yr}^{-1}$). The models of [Ref. 46] suggest that such systems should have a very low peak amplitude (barely consistent with the lower limit for HFF14Spo) and a low peak luminosity (~ 100 times less luminous than the HFF14Spo events).

The closest analog for the HFF14Spo events from the population of known RN systems is the nova M31N 2008-12a. [Ref. 85] provided a theoretical model that can account for the key observational characteristics of this remarkable nova: the very rapid recurrence timescale (<1 yr), fast optical light curve ($t_2 \sim 2$ days), and short supersoft x-ray phase (6-18 days after optical outburst)⁸³. To match these observations, [Ref. 85] invoke a $1.38 M_{\odot}$ white dwarf primary, drawing mass from a companion at a rate of $1.6 \times 10^{-7} M_{\odot} \text{ yr}^{-1}$. This is largely consistent with the theoretical expectations derived by [Ref. 46], and reinforces the conclusion that a combination of a high-mass white dwarf and efficient mass transfer are the key ingredients for rapid recurrence and short light curves. The one feature that cannot be effectively explained with this hypothesis is the peculiarly high luminosity of the HFF14Spo events – even after accounting for the very large uncertainties.

Expected Timescale for Microlensing Events. A commonly observed example of microlensing-induced transient effects is when a bright background source (a quasar) is magnified by a galaxy-scale lens^{93,94}. In this optically thick microlensing regime, the lensing potential along the line of sight to the quasar is composed of many stellar-mass objects. Each compact object along the line of sight generates a separate critical lensing curve, resulting in a complex web of overlapping critical curves. As all of these lensing stars are in motion relative to the background source, the web of caustics will shift across the source position, leading to a stochastic variability on timescales of months to years. This scenario is inconsistent with the observed data, as the two HFF14Spo events were far too short in duration and did not exhibit the repeated “flickering” variation that would be expected from optically thick microlensing.

For the cluster-scale lens relevant in the case of HFF14Spo, we should expect to be in the optically thin microlensing regime. This situation is similar to the “local” microlensing light curves observed when stars within our Galaxy or neighboring dwarf galaxies pass behind a massive compact halo object⁹⁵⁻⁹⁸. In this case, an isolated microlensing event can occur if there is a background star (i.e., in the HFF14Spo host galaxy) that is the dominant source of luminosity in its environment. In practice this means that the source must be a very bright O or B star with mass of order

Table 2. Properties of the local stellar population in the HFF14Spo host galaxy, from SED fitting.

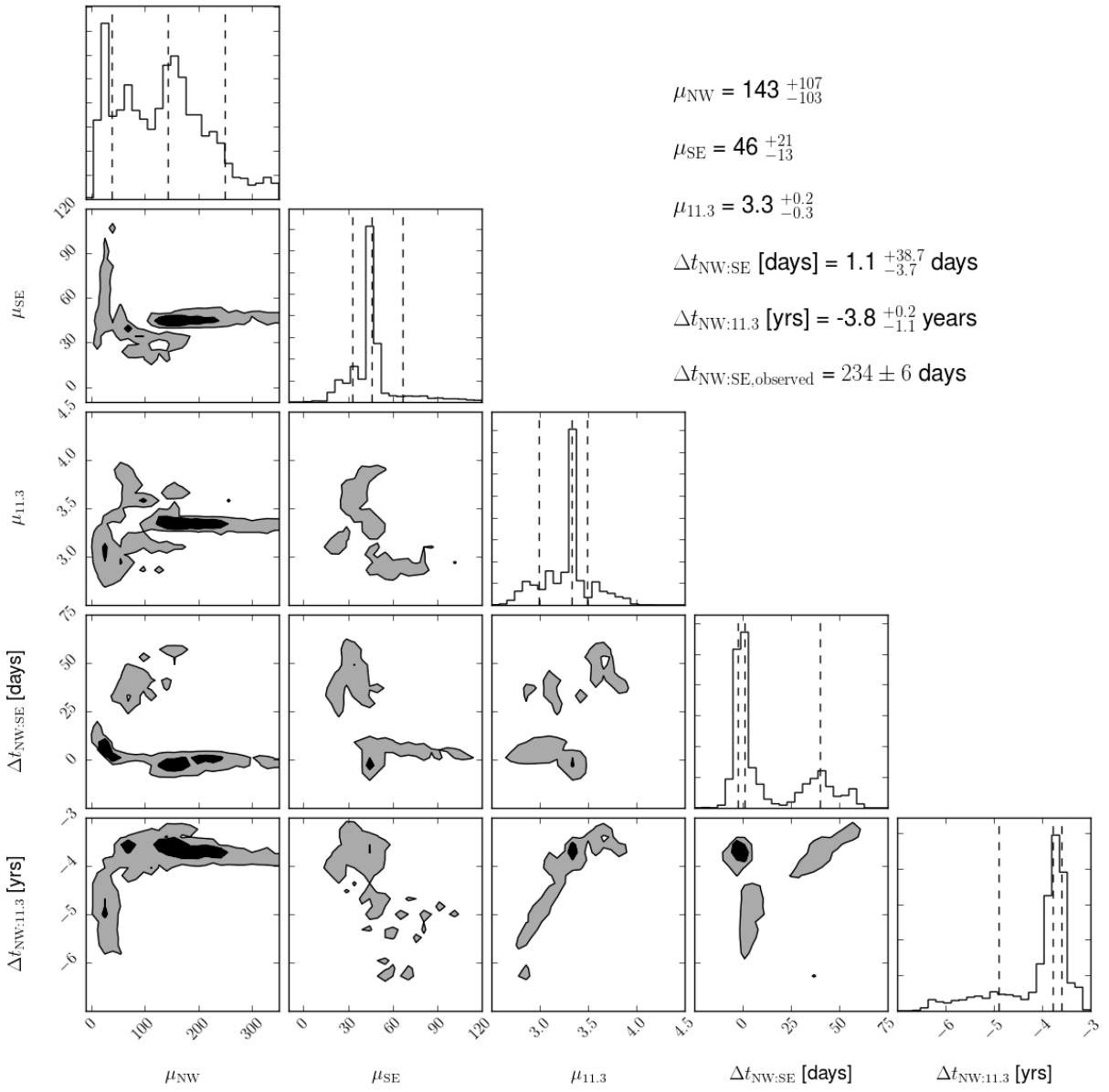
Host image:	11.1	11.2	11.3
Location:	HFF14Spo-SE	HFF14Spo-NW	center
$(U - V)_{\text{rest}}$	$0.69^{+0.2}_{-0.05}$	$0.52^{+0.15}_{-0.10}$	0.39 ± 0.05
$\log[\Sigma(M_*/M_\odot)]$	7.14 ± 0.15	7.14 ± 0.15	7.04 ± 0.10
Age (Gyr)	0.292 ± 0.5	0.290 ± 0.5	0.292 ± 0.5

$10 M_\odot$. Depending on its age, the size of such a star would range from a few to a few dozen times the size of the Sun. The net relative transverse velocity would be on the order of a few 100 km s^{-1} , which is comparable to the orbital velocity of stars within a galaxy or galaxies within a cluster.

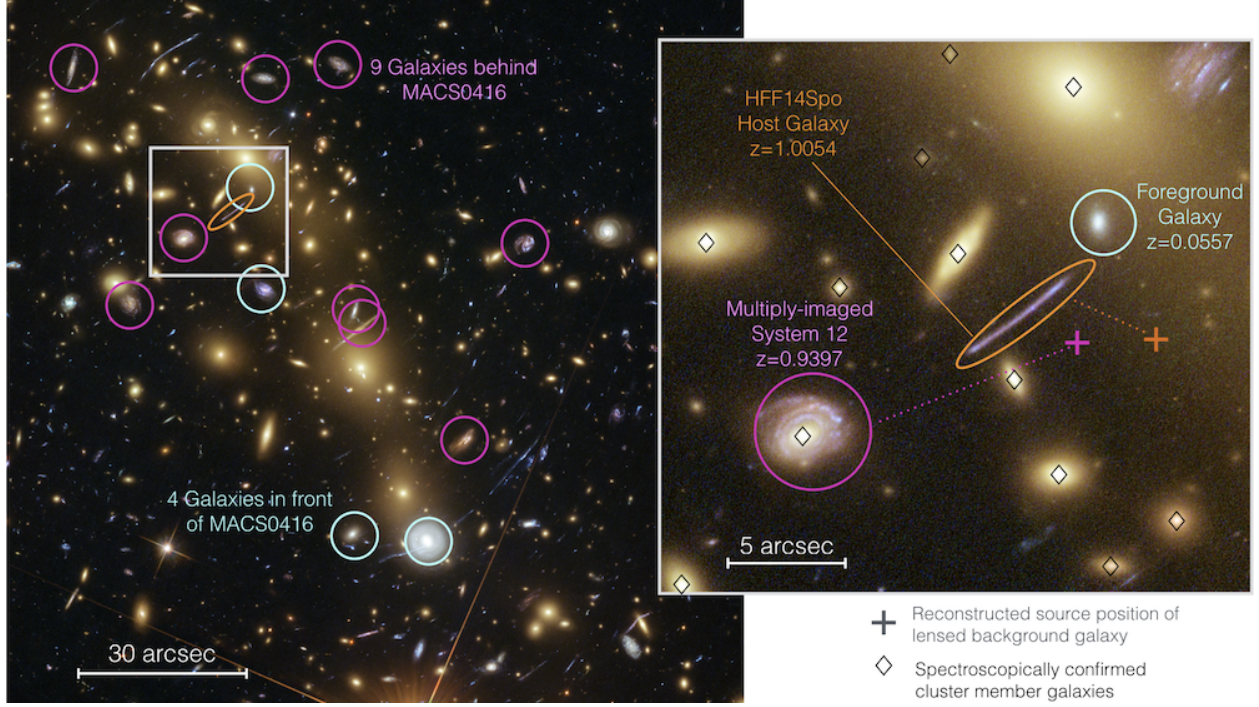
In the case of a smooth cluster potential, the timescale τ for the light curve of such a caustic crossing event is dictated by the radius of the source, R , and the net transverse velocity, v , of the source across the caustic^{48,99,100} as

$$\tau = \frac{6R}{5 R_\odot} \frac{300 \text{ km s}^{-1}}{v} \text{ hr.} \quad (3)$$

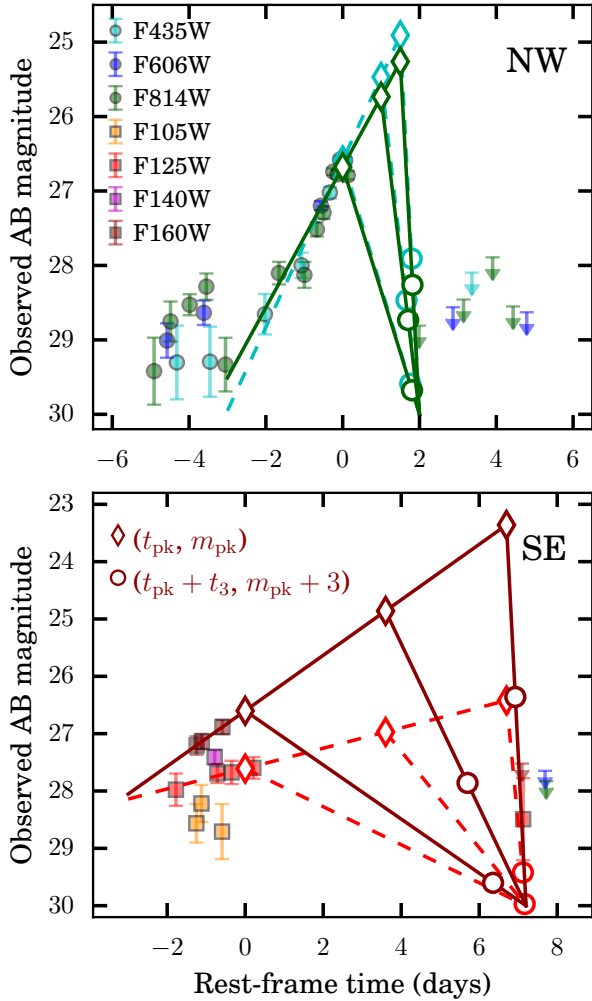
Thus, for reasonable assumptions about the star's radius and velocity, the timescale τ is on the order of hours to days, which is well matched to the observed rise and decline timescales of the HFF14Spo events.



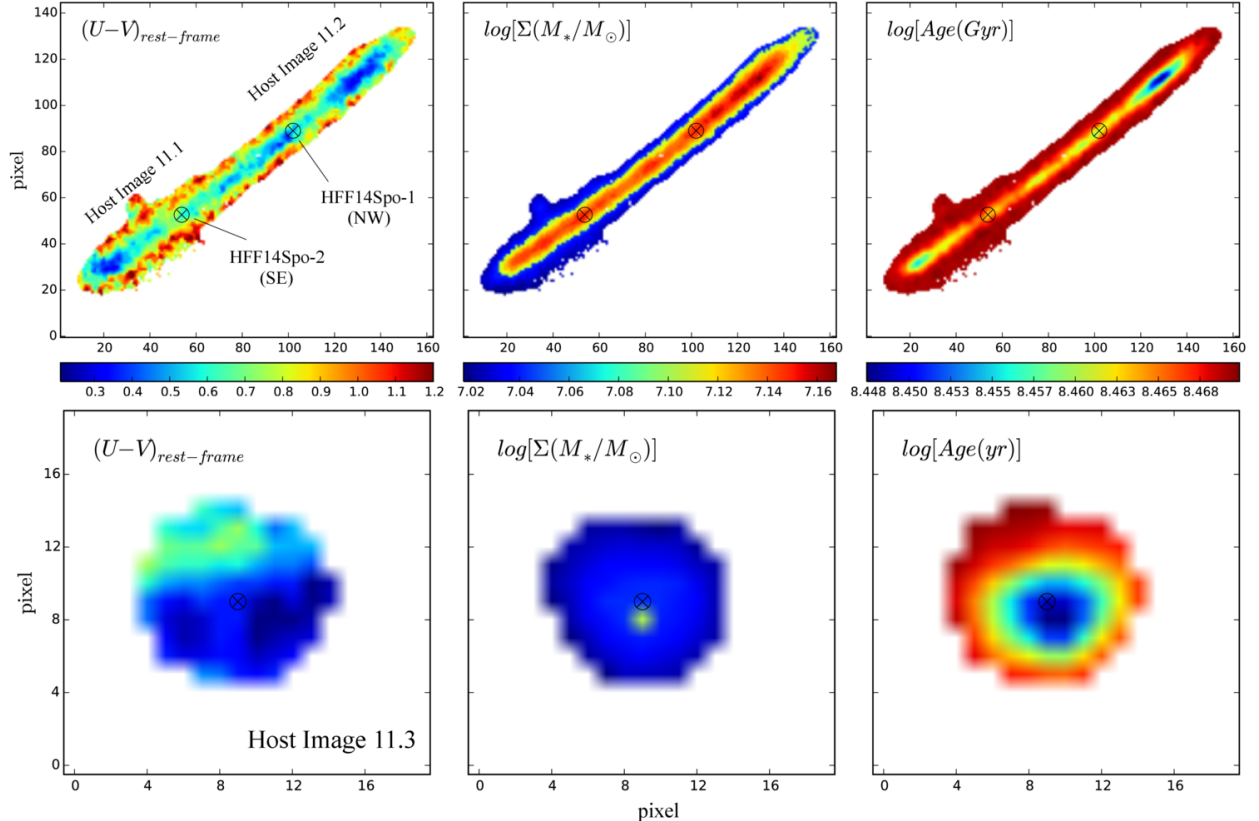
Supplementary Figure 1: Probability distributions for the five primary magnification and time-delay observables, drawn from a combination of results from five of our seven baseline lens models: CATS, GLAFIC, GLEE, GRALE, and ZLTM. Contours shown in the ten panels at the lower left mark the 1σ and 2σ confidence regions in each two-dimensional slice of the parameter space. Histograms at the top of each column show the marginalized 1-D probability distributions, with dashed vertical lines marking the mean and 1σ confidence region. These mean values and uncertainties are also reported in the table of values at the upper right. The final line in the table reports the observed time gap in days between HFF14Spo-NW in January, 2014 and HFF14Spo-SE in August, 2014.



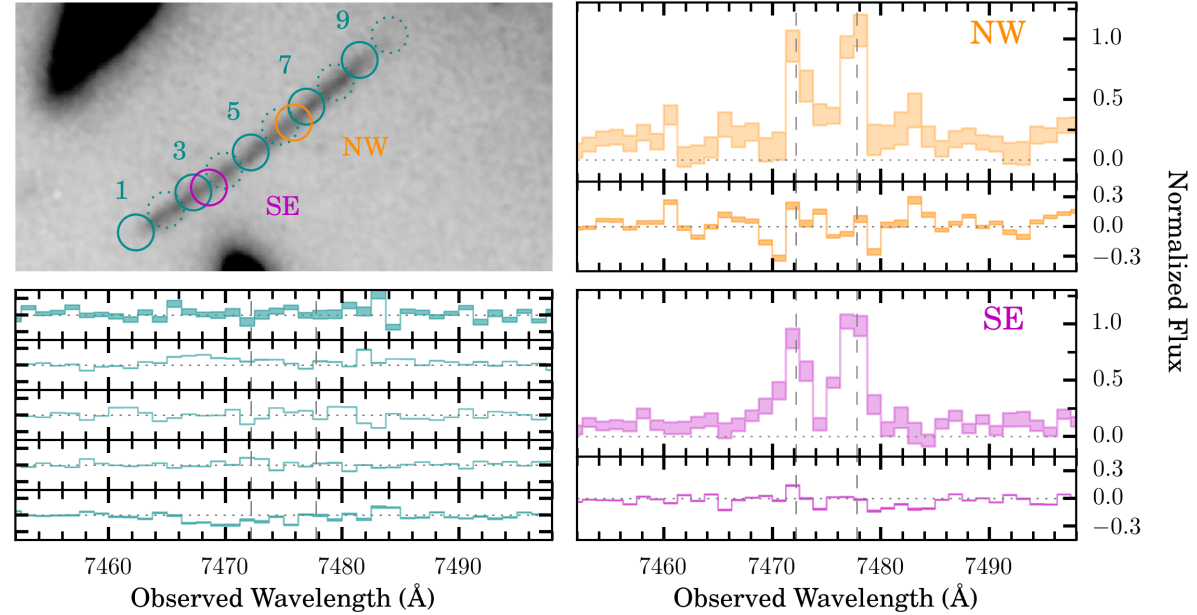
Supplementary Figure 2: Galaxies in the foreground and background of the MACS0416 cluster that are included in the GLEE-var model, which is a variation of the GLEE model that accommodates multi-plane lensing. The larger panel at left marks nine galaxies with spectroscopic redshifts greater than the cluster redshift (magenta circles) and four galaxies in the cluster foreground (light-blue circles). The inset panel at right zooms in on the HFF14Spo host galaxy (enclosed by the orange ellipse in each panel). Cluster member galaxies with spectroscopic redshifts that were included in the GLEE models are marked with black diamonds. The magenta circle marks a spiral galaxy at $z = 0.9397$, which is also strongly lensed by the MACS0416 cluster into three highly distorted images (System 12 in [Ref. 6]). This image of the System 12 galaxy is further strongly lensed into arcs around a cluster member galaxy, which is marked by the black diamond near the center of the magenta circle. The galaxy in the foreground of the cluster at $z = 0.0557$ is encircled in light blue. Crosses mark the reconstructed source positions (from the GLEE model) for the $z = 0.9397$ galaxy and the HFF14Spo host.



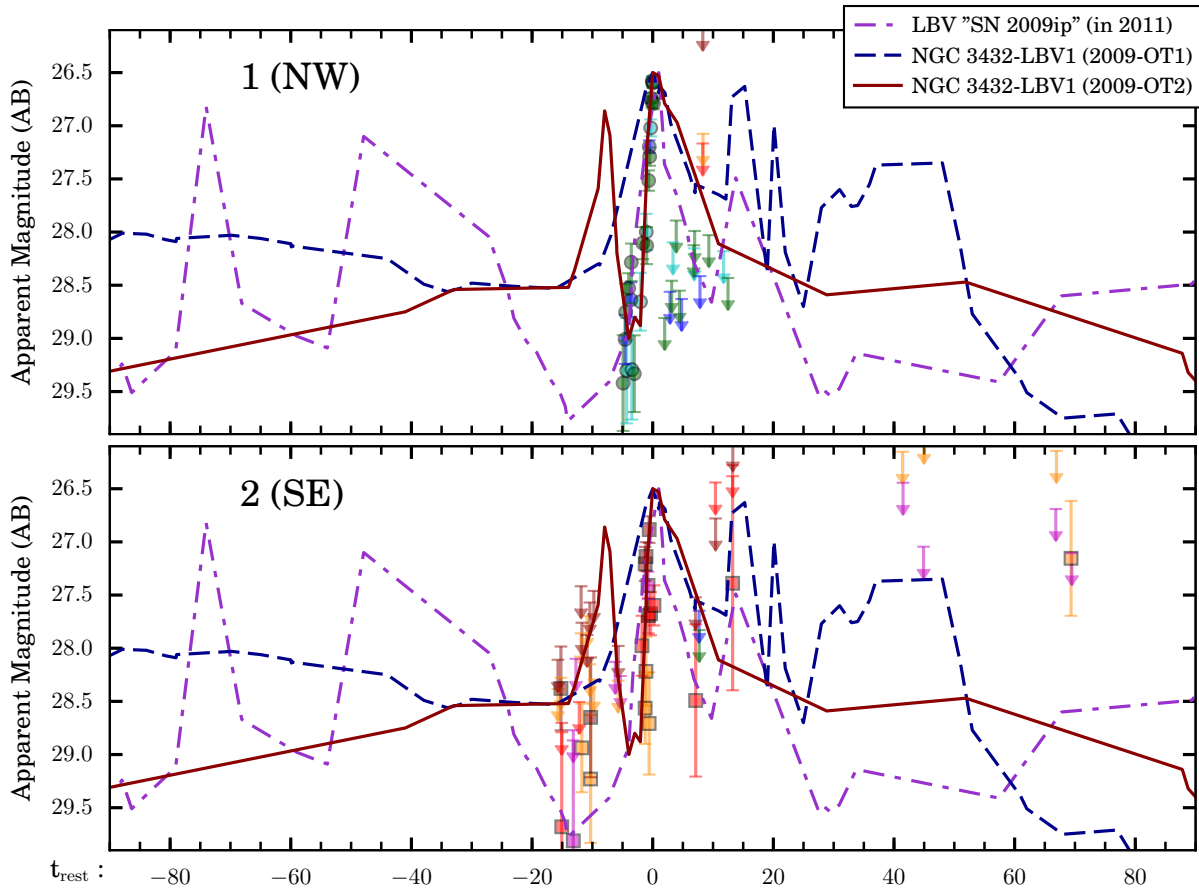
Supplementary Figure 3: Piecewise linear fits to the HFF14Spo light curves, used to measure the rise time and decay time of the two events. The HFF14Spo-NW light curve is shown in the top panel, and HFF14Spo-SE in the bottom. Filled points with error bars plot the observed brightness of each event in AB magnitudes as a function of rest-frame time (for $z = 1.0054$). Piecewise linear fits are shown for the four bands that have enough points for fitting: in the top panel fits are plotted for the F814W band (solid green lines) and the F435W band (dashed cyan lines), while in the bottom panel fits are shown for F160W (solid maroon) and F125W (dashed scarlet). Open diamonds in each panel show three examples of assumptions for the time of peak brightness, t_{pk} (i.e., the position where the rising piece of the linear fit ends). Open circles mark the corresponding point, $t_{pk} + t_3$, at which the fading transient would have declined in brightness by 3 mag. See text for details on the fitting procedure.



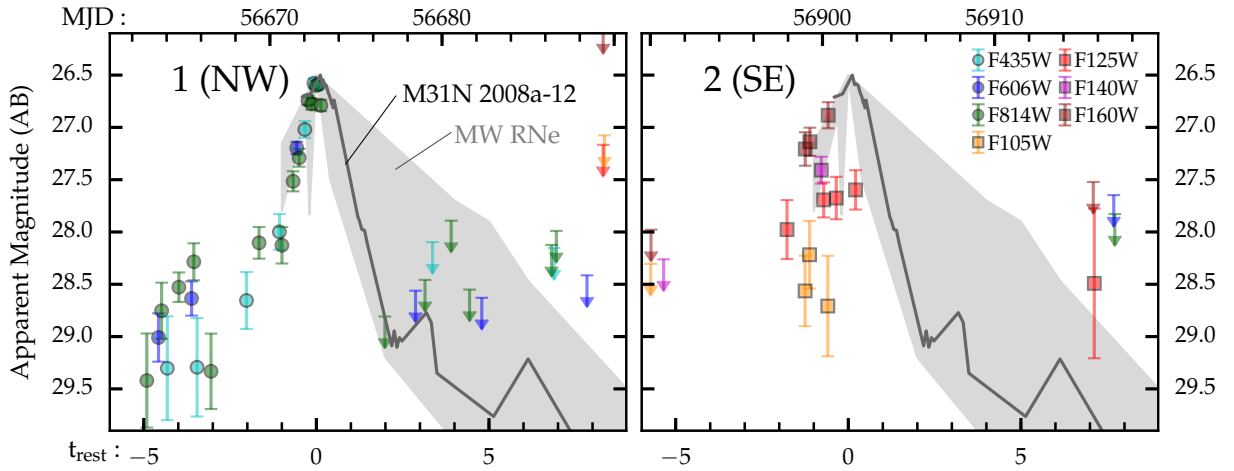
Supplementary Figure 4: Stellar population properties of the HFF14Spo host galaxy, derived from “pixel-by-pixel” SED fitting. The top row shows maps for the adjacent host images 11.1 and 11.2, and the bottom panels show image 11.3. From left to right the panels present the rest-frame ($U-V$) color, the stellar surface mass density Σ , and the mean age of the stellar population in Gyr. Markers in the top row denote the positions of the two HFF14Spo transient events. Markers in the bottom panels are at the center of host image 11.3.



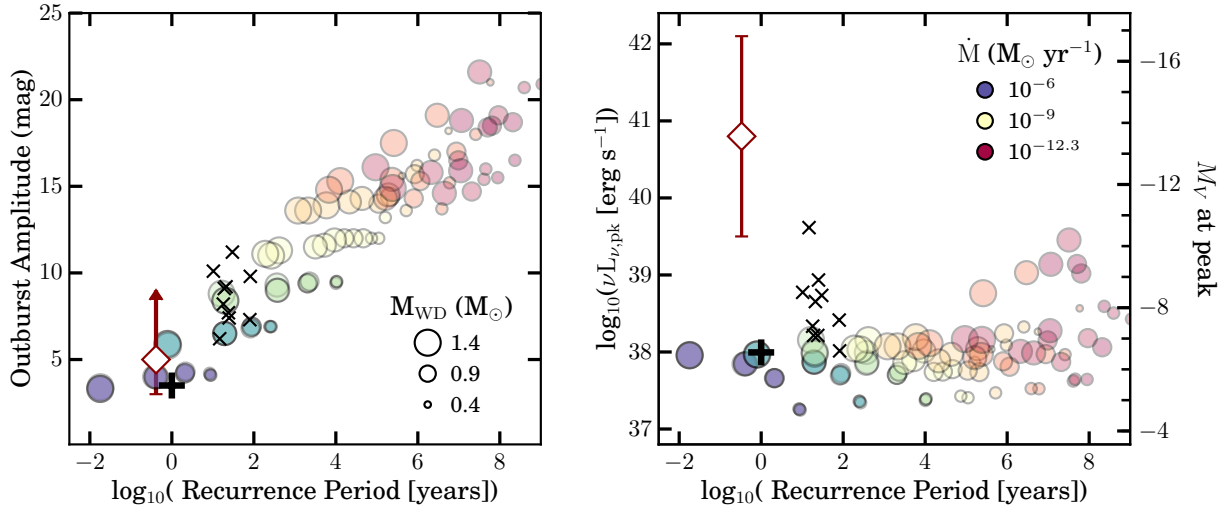
Supplementary Figure 5: Measurements of the [OII] $\lambda\lambda 3726, 3729$ doublet, observed with MUSE after both HFF14Spo events had faded. The upper-left panel shows the 12 apertures with radius $0.6''$ that were used for the extractions reported in Table 1. Odd-numbered apertures are plotted with solid lines, while even-numbered apertures are shown as unlabeled dashed circles. The apertures centered on the HFF14Spo-NW and SE locations are highlighted in orange and magenta, respectively. The 1-D spectra extracted from these HFF14Spo locations are shown in the upper-right and lower-right panels, centered around the observed wavelength of the [OII] doublet, and normalized to reach a value of unity at the peak of the $\lambda 3729$ line. Dashed vertical lines mark the vacuum wavelengths of the doublet, redshifted to $z = 1.0054$. The width of the shaded region indicates the 1σ uncertainty in the measured flux. Below each spectrum, a residual plot shows the flux that remains after subtracting off a mean spectrum constructed from the normalized spectra of the odd-numbered apertures. The lower-left panel shows the same residual spectra constructed for the odd-numbered apertures, demonstrating that the [OII] line profile does not exhibit any significant gradients across the length of the host-galaxy arc.



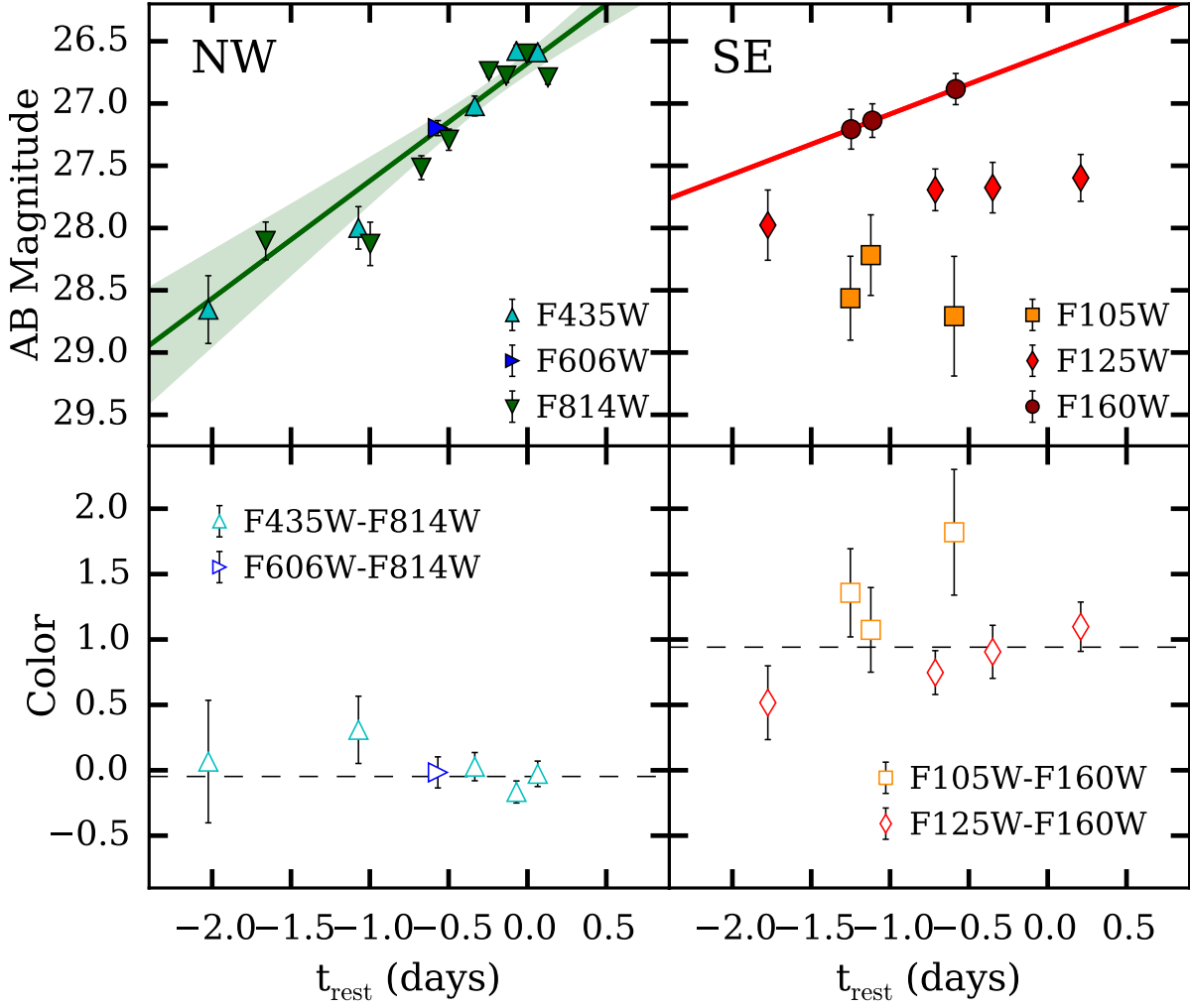
Supplementary Figure 6: Comparison of observed HFF14Spo light curves against rapid outbursts from two LBVs. Colored markers show the HFF14Spo light-curve data, as in Figure 4, with downward arrows marking 3σ upper limits in epochs with no detection of the HFF14Spo source. The LBV comparison light curves have been shifted in time and magnitude to match up with the peak of the observed light curves.



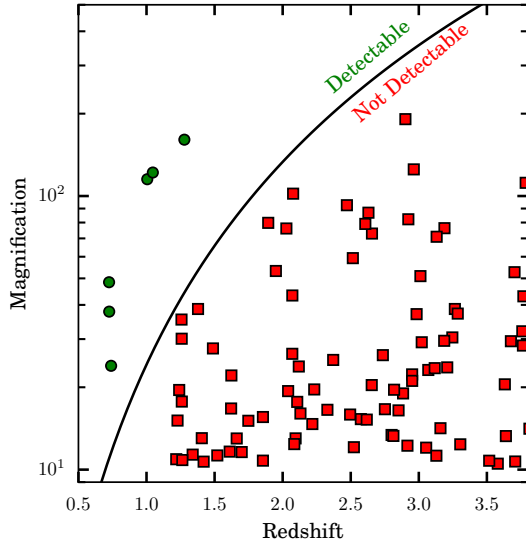
Supplementary Figure 7: Comparison of the HFF14Spo light curves against template light curves for RN outbursts. Colored markers show the HFF14Spo light-curve data, as in Figure 4, plotting the apparent magnitude as a function of time in the rest frame (bottom axis) and observer frame (top axis). The gray shaded regions encompass the outburst light-curve shapes of 5 of the 11 known Galactic RNe (U Sco, V2487 Oph, V394 CrA, T CrB, and V745 Sco), selected because they exhibit a rapid decline in their light curves⁴⁰. The solid black line traces the 2014 outburst light-curve shape for the rapid-recurrence nova M31N 2008a-12⁴². All template light curves have been normalized to match the observed peaks of the HFF14Spo events.



Supplementary Figure 8: Comparison of the inferred HFF14Spo recurrence timescale against observed RNe and models. In the left panel the outburst amplitude in magnitudes is plotted against the recurrence timescale, while in the right panel the ordinate axis shows the peak luminosity (or absolute magnitude). In both panels, the joint constraints on HFF14Spo from both transient episodes are plotted as large open diamonds, observed constraints from the 10 Galactic RNe appear as black “x” points, and the rapid-recurrence nova M31N 2008a-12 is shown with a thick black “+” marker. Colored circles show the results from a suite of numerical hydrodynamic simulations⁴⁶. The size of each circle indicates the mass of the primary white dwarf (WD) star over the range $0.4-1.4 M_{\odot}$, as indicated in the legend of the left panel. The color of each circle denotes the rate of mass transfer from the secondary onto the WD, as given in the right panel’s legend.



Supplementary Figure 9: Observed colors for the HFF14Spo events. Filled points plotted in the top panels show observed AB magnitudes for the HFF14Spo-NW and HFF14Spo-SE events from 3 rest-frame days before the date of observed peak brightness. Solid lines and shaded regions show linear fits to the data in the F814W and F160W bands. Open points in the bottom panels show observed colors in the rest-frame bands. For each color the magnitude in the bluer band is the directly measured value, and the magnitude in the redder band is interpolated from the linear fits shown in the top panel. All colors are consistent with showing no evolution over the rising portion of each light curve.



Supplementary Figure 10: Model-predicted magnification and redshift for strongly lensed galaxies behind all six of the HFF clusters (Abell 2744, Abell 370, Abell S1063, MACS J1149, MACS J0416, and MACS J0717). The black curve shows the minimum magnification required to make a HFF14Spo-like transient detectable, as a function of redshift. To define the distance modulus as a function of redshift for this curve, a standard Λ CDM cosmological model is adopted¹⁰¹. Green circles above the line represent the six galaxies in which a transient with $M_V > -14$ mag would be sufficiently magnified, and red squares below the line mark all the other galaxies in which the HFF14Spo events would not have been detected.

Table 3. Photometry of the HFF14Spo-NW event.

Date (MJD)	Filter	Flux Density (10^{30} erg s $^{-1}$ cm $^{-2}$ Hz $^{-1}$)	AB Mag
56144.86	F105W	0.063±0.119	<29.39
56184.90	F105W	-0.013±0.178	<27.08
56689.43	F105W	-0.111±0.179	<27.08
56869.98	F105W	-0.001±0.075	<28.01
56870.98	F105W	0.068±0.048	<29.32
56877.68	F105W	-0.084±0.111	<27.59
56877.94	F105W	0.005±0.051	<32.09
56879.67	F105W	0.008±0.048	<31.71
56880.60	F105W	-0.003±0.057	<28.32
56880.86	F105W	-0.002±0.067	<28.14
56881.92	F105W	-0.065±0.100	<27.71
56890.02	F105W	-0.063±0.103	<27.68
56898.99	F105W	-0.005±0.079	<27.96
56899.25	F105W	0.001±0.083	<34.33
56900.31	F105W	0.014±0.067	<31.02
56984.58	F105W	-0.152±0.434	<26.11
56991.68	F105W	-0.242±0.396	<26.21
57035.72	F105W	0.172±0.202	<28.31
57040.57	F105W	0.460±0.211	27.24±0.50
56132.22	F110W	0.066±0.046	<29.35
56170.80	F110W	-0.179±0.251	<26.71
56159.62	F125W	-0.124±0.208	<26.91
56197.80	F125W	0.228±0.143	<28.00
56689.36	F125W	0.028±0.165	<30.27
56871.26	F125W	-0.037±0.069	<28.11
56877.09	F125W	0.010±0.048	<31.43
56897.94	F125W	-0.008±0.102	<27.69
56900.07	F125W	-0.063±0.116	<27.55
56900.80	F125W	0.089±0.060	<29.02
56901.92	F125W	0.061±0.056	<29.43
56915.79	F125W	0.024±0.125	<30.43
56922.36	F125W	0.393±0.360	<27.41
56928.07	F125W	0.095±0.166	<28.96
56159.63	F140W	-0.144±0.256	<26.69

Table 3 (cont'd)

Date (MJD)	Filter	Flux Density (10^{30} erg s $^{-1}$ cm $^{-2}$ Hz $^{-1}$)	AB Mag
56184.88	F140W	-0.103±0.186	<27.03
56875.10	F140W	-0.026±0.067	<28.14
56875.97	F140W	0.008±0.042	<31.70
56889.05	F140W	-0.019±0.081	<27.94
56890.77	F140W	-0.181±0.158	<27.21
56899.93	F140W	-0.126±0.148	<27.28
56984.72	F140W	-0.105±0.266	<26.65
56991.55	F140W	0.202±0.160	<28.14
57035.52	F140W	-0.272±0.393	<26.22
57040.83	F140W	0.004±0.239	<32.32
56132.24	F160W	-0.280±0.401	<26.20
56144.87	F160W	0.001±0.267	<34.03
56170.79	F160W	0.104±0.185	<28.85
56197.79	F160W	-0.239±0.332	<26.40
56689.36	F160W	-0.400±0.485	<25.99
56870.00	F160W	0.083±0.067	<29.10
56870.99	F160W	0.257±0.108	27.88±0.46
56877.70	F160W	-0.048±0.128	<27.44
56877.96	F160W	-0.008±0.101	<27.70
56879.69	F160W	-0.009±0.080	<27.95
56880.61	F160W	0.035±0.069	<30.05
56880.88	F160W	-0.185±0.239	<26.76
56881.94	F160W	-0.070±0.141	<27.34
56890.04	F160W	-0.111±0.152	<27.26
56899.00	F160W	-0.064±0.141	<27.33
56899.27	F160W	-0.147±0.176	<27.09
56900.33	F160W	-0.014±0.122	<27.50
56915.73	F160W	-0.021±0.208	<26.91
56922.41	F160W	-0.120±0.313	<26.47
56928.13	F160W	-0.186±0.352	<26.34
56159.54	F435W	0.012±0.016	<31.23
56184.77	F435W	-0.001±0.010	<30.23
56664.04	F435W	0.069±0.031	29.30±0.50
56665.77	F435W	0.070±0.030	29.29±0.47

Table 3 (cont'd)

Date (MJD)	Filter	Flux Density (10^{30} erg s $^{-1}$ cm $^{-2}$ Hz $^{-1}$)	AB Mag
56668.64	F435W	0.125±0.031	28.66±0.27
56670.55	F435W	0.229±0.036	28.00±0.17
56672.03	F435W	0.565±0.041	27.02±0.08
56672.56	F435W	0.849±0.035	26.58±0.05
56672.83	F435W	0.840±0.038	26.59±0.05
56679.45	F435W	-0.065±0.070	<28.10
56686.51	F435W	-0.056±0.066	<28.15
56696.27	F435W	-0.030±0.065	<28.18
56144.78	F606W	-0.021±0.017	<30.59
56170.73	F606W	-0.117±0.110	<29.89
56663.53	F606W	0.090±0.019	29.01±0.23
56665.45	F606W	0.127±0.019	28.64±0.16
56671.56	F606W	0.480±0.027	27.20±0.06
56678.46	F606W	-0.059±0.046	<28.56
56682.31	F606W	-0.060±0.043	<28.63
56688.42	F606W	-0.067±0.052	<28.41
56916.92	F606W	-0.020±0.064	<28.20
56144.80	F814W	0.314±0.317	<27.66
56157.83	F814W	0.028±0.041	<30.29
56170.72	F814W	-0.108±0.109	<27.61
56184.75	F814W	0.004±0.007	<32.47
56662.85	F814W	0.062±0.026	29.42±0.45
56663.71	F814W	0.114±0.028	28.75±0.27
56664.71	F814W	0.141±0.018	28.53±0.14
56665.58	F814W	0.176±0.029	28.28±0.18
56666.58	F814W	0.067±0.022	29.33±0.36
56669.37	F814W	0.208±0.029	28.10±0.15
56670.70	F814W	0.204±0.033	28.13±0.17
56671.35	F814W	0.358±0.032	27.52±0.10
56671.70	F814W	0.440±0.034	27.29±0.09
56672.21	F814W	0.731±0.031	26.74±0.05
56672.43	F814W	0.707±0.036	26.78±0.06
56672.69	F814W	0.832±0.035	26.60±0.05
56672.96	F814W	0.698±0.035	26.79±0.06

Table 3 (cont'd)

Date (MJD)	Filter	Flux Density (10^{30} erg s $^{-1}$ cm $^{-2}$ Hz $^{-1}$)	AB Mag
56676.68	F814W	0.019±0.036	<30.68
56679.01	F814W	-0.015±0.050	<28.46
56680.53	F814W	-0.109±0.084	<27.89
56681.60	F814W	-0.021±0.046	<28.55
56686.36	F814W	-0.053±0.068	<28.12
56686.64	F814W	-0.092±0.077	<27.99
56691.36	F814W	-0.074±0.074	<28.03
56697.73	F814W	-0.040±0.051	<28.43
56916.98	F814W	0.007±0.093	<31.86

Table 4. Photometry of the HFF14Spo-SE event.

Date (MJD)	Filter	Flux Density (10^{30} erg s $^{-1}$ cm $^{-2}$ Hz $^{-1}$)	AB Mag
56144.86	F105W	-0.127±0.206	<26.92
56184.90	F105W	0.120±0.169	<28.70
56689.43	F105W	-0.100±0.170	<27.13
56869.98	F105W	0.041±0.054	<29.88
56870.98	F105W	0.009±0.059	<31.56
56877.68	F105W	-0.031±0.087	<27.86
56877.94	F105W	0.097±0.037	28.94±0.42
56879.67	F105W	-0.078±0.101	<27.70
56880.60	F105W	-0.022±0.066	<28.15
56880.86	F105W	0.074±0.041	<29.23
56881.92	F105W	0.034±0.058	<30.06
56890.02	F105W	0.046±0.058	<29.73
56898.99	F105W	0.136±0.042	28.56±0.34
56899.25	F105W	0.187±0.056	28.22±0.32
56900.31	F105W	0.119±0.053	28.71±0.48
56984.58	F105W	-0.151±0.419	<26.15
56991.68	F105W	-0.404±0.498	<25.96
57035.72	F105W	-0.265±0.422	<26.14
57040.57	F105W	0.499±0.248	27.15±0.54
56132.22	F110W	0.050±0.045	<29.64
56170.80	F110W	-0.230±0.307	<26.49
56159.62	F125W	-0.329±0.387	<26.24
56197.80	F125W	-0.226±0.310	<26.48
56689.36	F125W	-0.076±0.190	<27.01
56871.26	F125W	0.049±0.040	<29.68
56877.09	F125W	0.009±0.048	<31.51
56897.94	F125W	0.234±0.061	27.98±0.28
56900.07	F125W	0.304±0.047	27.69±0.17
56900.80	F125W	0.309±0.058	27.68±0.20
56901.92	F125W	0.332±0.058	27.60±0.19
56915.79	F125W	0.146±0.096	<28.49
56922.36	F125W	-0.275±0.321	<26.44
56928.07	F125W	0.402±0.373	<27.39
56159.63	F140W	-0.006±0.159	<27.21

Table 4 (cont'd)

Date (MJD)	Filter	Flux Density (10^{30} erg s $^{-1}$ cm $^{-2}$ Hz $^{-1}$)	AB Mag
56184.88	F140W	-0.077±0.168	<27.14
56875.10	F140W	0.043±0.038	<29.81
56875.97	F140W	-0.045±0.070	<28.10
56889.05	F140W	0.042±0.068	<29.85
56890.77	F140W	0.055±0.060	<29.55
56899.93	F140W	0.395±0.047	27.41±0.13
56984.72	F140W	-0.226±0.320	<26.44
56991.55	F140W	0.003±0.184	<32.56
57035.52	F140W	-0.068±0.255	<26.69
57040.83	F140W	0.142±0.174	<28.52
56132.24	F160W	-0.196±0.355	<26.33
56144.87	F160W	-0.592±0.716	<25.57
56170.79	F160W	-0.375±0.461	<26.05
56197.79	F160W	-0.766±0.725	<25.56
56689.36	F160W	-0.282±0.405	<26.19
56870.00	F160W	0.028±0.069	<30.30
56870.99	F160W	0.162±0.059	28.38±0.39
56877.70	F160W	-0.047±0.131	<27.42
56877.96	F160W	-0.002±0.095	<27.76
56879.69	F160W	0.004±0.086	<32.34
56880.61	F160W	-0.043±0.113	<27.57
56880.88	F160W	0.126±0.065	<28.65
56881.94	F160W	-0.026±0.125	<27.46
56890.04	F160W	0.035±0.078	<30.05
56899.00	F160W	0.476±0.070	27.21±0.16
56899.27	F160W	0.507±0.063	27.14±0.13
56900.33	F160W	0.640±0.074	26.88±0.12
56915.73	F160W	0.053±0.119	<29.59
56922.41	F160W	0.037±0.235	<29.99
56928.13	F160W	-0.281±0.466	<26.04
56159.54	F435W	0.002±0.007	<33.06
56184.77	F435W	-0.009±0.013	<29.93
56664.04	F435W	0.033±0.034	<30.11
56665.77	F435W	-0.019±0.039	<28.73

Table 4 (cont'd)

Date (MJD)	Filter	Flux Density (10^{30} erg s $^{-1}$ cm $^{-2}$ Hz $^{-1}$)	AB Mag
56668.64	F435W	0.044±0.035	<29.79
56670.55	F435W	0.047±0.043	<29.71
56672.03	F435W	0.051±0.039	<29.63
56672.56	F435W	-0.046±0.065	<28.18
56672.83	F435W	-0.064±0.075	<28.01
56679.45	F435W	0.018±0.035	<30.74
56686.51	F435W	-0.026±0.052	<28.41
56696.27	F435W	0.009±0.049	<31.48
56144.78	F606W	0.234±0.176	<27.98
56170.73	F606W	0.043±0.061	<29.81
56663.53	F606W	0.004±0.027	<32.27
56665.45	F606W	0.016±0.026	<30.91
56671.56	F606W	-0.021±0.043	<28.61
56678.46	F606W	-0.012±0.029	<29.05
56682.31	F606W	-0.016±0.035	<28.83
56688.42	F606W	0.033±0.024	<30.10
56916.92	F606W	-0.121±0.106	<27.65
56144.80	F814W	-0.294±0.274	<26.61
56157.83	F814W	-0.025±0.146	<27.29
56170.72	F814W	-0.027±0.127	<27.45
56184.75	F814W	0.037±0.010	29.97±0.29
56662.85	F814W	0.026±0.036	<30.37
56663.71	F814W	-0.019±0.052	<28.42
56664.71	F814W	0.005±0.026	<32.15
56665.58	F814W	-0.056±0.072	<28.07
56666.58	F814W	-0.007±0.038	<28.75
56669.37	F814W	0.010±0.042	<31.44
56670.70	F814W	0.005±0.042	<32.12
56671.35	F814W	0.075±0.029	29.21±0.41
56671.70	F814W	0.209±0.156	<28.10
56672.21	F814W	-0.014±0.054	<28.38
56672.43	F814W	0.005±0.041	<32.14
56672.69	F814W	-0.003±0.036	<28.81
56672.96	F814W	-0.020±0.053	<28.41

Table 4 (cont'd)

Date (MJD)	Filter	Flux Density (10^{30} erg s $^{-1}$ cm $^{-2}$ Hz $^{-1}$)	AB Mag
56676.68	F814W	-0.005±0.042	<28.64
56679.01	F814W	0.016±0.040	<30.89
56680.53	F814W	-0.009±0.045	<28.57
56681.60	F814W	0.012±0.037	<31.22
56686.36	F814W	-0.031±0.055	<28.35
56686.64	F814W	-0.031±0.050	<28.45
56691.36	F814W	0.042±0.036	<29.84
56697.73	F814W	0.064±0.019	29.39±0.31
56916.98	F814W	-0.028±0.089	<27.83